PHYSICAL REVIEW C

NUCLEAR PHYSICS

THIRD SERIES, VOLUME 32, NUMBER 4 OCTOBER 1985

Shell-model analysis of high-resolution data for elastic and inelastic electron scattering on ^{19}F

B. A. Brown and B. H. Wildenthal*
Cyclotron Laboratory, Michigan State University, East Lansing, Michigan 48824

C. F. Williamson, F. N. Rad,† and S. Kowalski
Bates Linear Accelerator Center and Department of Physics, Massachusetts Institute of Technology, Cambridge, Massachusetts 02139

Hall Crannell
Department of Physics, Catholic University of America, Washington, D.C. 20064

J. T. O'Brien
Department of Physics and Geoscience, Montgomery College, Rockville, Maryland 20850
(Received 4 April 1985)

A comprehensive theoretical and experimental investigation of electron scattering on ^{19}F is presented. Theoretical procedures for calculating the various components of electron scattering form factors from multiparticle shell-model wave functions are summarized. These procedures are used to compare shell-model predictions with data from electron scattering on ^{19}F. For the positive-parity states of ^{19}F we use $1s0d$ shell-model wave functions obtained with a new "universal" Hamiltonian and for the negative-parity states we use $0p$-$1s0d$ shell-model wave functions based on the cross-shell Hamiltonian of Millener and Kurath. The comparisons are made with measured longitudinal and transverse form factors for momentum transfers up to 2.4 fm^{-1} which are extracted from experimental data obtained with electron energies from 78 to 340 MeV, and angles of 45°, 90°, and 160°. The energy resolution was 25–50 keV and most of the known levels below 8 MeV in excitation were resolved and compared with theory.

I. INTRODUCTION

In this paper we summarize procedures for calculating the various components of electron scattering form factors from conventional multiparticle shell-model wave functions. We then apply these procedures to compare recent experimental results on ^{19}F with the predictions from a new calculation of *sd*-shell nuclear structure. Earlier electron scattering experiments[1,2] on ^{19}F lacked the energy resolution to separate many of the excited states. Also lacking in previous work were the ranges of energy and angle necessary to map the transition densities over a wide range of momentum transfers and to separate the longitudinal and transverse components.

The present work marks significant advances in these areas. By using the high-resolution scattering facility[3,4] of the Bates Linear Accelerator Center, energy resolutions of 25–50 keV have been achieved and measurements have been made at momentum transfers up to 2.4 fm^{-1}. It has thus been possible to resolve about 41 levels below an excitation energy of 8 MeV. These data, which provide examples of both transverse and longitudinal excitations of multipolarity 1 through 4, measured over a broad range of momentum transfer, provide the material for a thorough examination of nuclear phenomena as revealed by electron scattering and of how these phenomena can be reproduced from wave functions obtained in shell-model calculations.

Many aspects of ^{19}F make this nucleus particularly interesting in terms of nuclear structure phenomena. It has stimulated progress in our understanding of the nuclear shell-model ever since the pioneering work of Elliott and Flowers[5] and Redlich.[6] Previous electron scattering experiments,[7,1,2,8] as well as measurements of electromagnetic transition strengths,[9–13] have indicated that ^{19}F is a nucleus whose ground and low-lying excited states are strongly deformed. In its spectrum groups of states have been tentatively identified as constituting rotational bands built upon both the $K^\pi=\frac{1}{2}^+$ ground state and the $K^\pi=\frac{1}{2}^-$ first excited state. Many additional states, of both positive and negative parity, are experimentally iden-

tified in the lowest 8 MeV of excitation energy.

The fact that ^{19}F corresponds in the simple shell model to a system of only three active nucleons outside the ^{16}O core and, as remarked, shows evidence of strong deformations, suggests a remarkable synthesis of these deformations out of a small number of shell-model configurations. The simplicity of this shell-model foundation lends itself to the study of the microscopic origins of nuclear deformations. At the same time, the essential degeneracy of the $\frac{1}{2}^+$ ground and $\frac{1}{2}^-$ first-excited states illustrates the susceptibility of this $N=10$, $Z=9$ system to the breaking of the $N=Z=8$ "magic number" core. Some negative-parity excitations can also be treated microscopically, and thus there is the chance in ^{19}F to study deformations which arise out of negative-parity "particle-hole" excitations simultaneously with those stemming from "particles-only" excitations.

Finally, the interplay of the closed-core and the excited-core configurations in ^{19}F make it an excellent laboratory in which to study the coexistence of "orthodox" shell-model states and "intruder" states of the same parity. Further away from the shell-closure boundaries, the states in the low-energy portion of the excitation energy spectra seem to be dominated by the orthodox configurations constructed from the orbits of the conventional shell-model space. For the *sd* shell the conventional space consists of the $0d_{5/2}$, $1s_{1/2}$, and $0d_{3/2}$ orbits. In ^{19}F, the relative simplicity of the spectrum of excitations which can be legitimately generated out of this space as compared to the complexity of the observed spectrum makes it apparent that many of the positive-parity states observed in the low-energy portion of the experimental spectrum must have their origins outside of the *sd*-shell space. Presumably, the presence of these intruder states at low excitation energies is to be associated with the proximity of ^{19}F to the ^{16}O shell boundary. An understanding of these neighboring intruder excitations and their effects upon the structural details of the orthodox states are fundamental to understanding the viability of the nuclear shell model.

Experimental procedures by which the present data were obtained are discussed in Sec. II. The reduction of the spectra to longitudinal and transverse form factors for individual states is discussed in Sec. III. In Sec. IV, the general theoretical formulation for electron scattering form factors in a spherical shell-model basis is presented. In Sec. V, we discuss the theoretical formulations of the ^{19}F wave functions which we use here, along with the approximations we use to calculate the transition densities and form factors. Comparison between experiment and theory is made in Sec. VI and our conclusions are summarized in Sec. VII.

II. EXPERIMENTAL PROCEDURE

Electrons of energies from 78 to 340 MeV, produced by the Bates Linear Accelerator,[14] were used for this experiment. The electron beam was carried about 75 m from the accelerator to the target area by a magnetic transport system that presented a space-focused beam on the target which had a momentum dispersion of about 7 cm/%. The beam spot on the target was typically 25 mm high and 3 mm wide.

The targets used in this experiment were sheets of Teflon[15] of average thickness 16—40 mg/cm^2 as determined by weighing a known area on a precision balance. Since this material is not physically stable under intense electron bombardment, the effective beam current per unit area was greatly reduced by spinning a 10 cm diam sheet of the material in the beam at the rate of three to five revolutions/sec. With this technique it proved feasible to use average beam currents of 8—12 μA on the Teflon targets for extended periods of time.

It was discovered early in the experimental work that the useful lifetime of the Teflon targets was strongly related to the duty cycle of the accelerator. For the same average current, a peak current of 5 mA would normally result in target failure in about two hours, whereas a peak current of 1.5 mA would typically result in a useful target lifetime greater that 24 hours. By keeping the accelerator peak current below 2 mA, it was normally possible to complete a 72-hour run with three targets while running an average beam current of 8—12 μA.

The ratio of ^{19}F to ^{12}C in the Teflon targets was monitored as a function of time to determine if there were chemical changes in the target due to electron bombardment. This ratio was never observed to vary by more than 2%, as determined by the areas of the elastic scattering peaks. The physical changes in the targets, such as embrittlement, appeared to be due to changes in the polymer linkages and not due to differential loss of the constituents.

The integrated beam current was measured by a nonintercepting ferrite monitor[16] which had been calibrated by the National Bureau of Standards against a standard Faraday cup to absolute accuracy of about 0.1%. This calibration was checked on a routine basis by a precision pulser feeding into a one-turn current loop wound onto the toriod.

The MIT energy-loss spectrometer and focal-plane detector system which were used in this experiment are described in detail elsewhere.[3,4] An absolute resolution of 25—50 keV was attained in this experiment at a solid angle of 3.3 msr with a useful momentum range of 5%. Data were taken at laboratory scattering angles of 45°, 90°, and 160°. At 45° and 90° the target angle was set so that the normal to its surface bisected the scattering angle. In this geometry all electrons arriving at the spectrometer have traversed the same thickness of target, so that only the straggling about the average energy loss of the beam contributed to the peak width. At 160°, the steepness of the angle of incidence precluded the use of this technique, and the target was set so that its surface normal bisected the supplement of the scattering angle. This resulted in somewhat poorer momentum resolution at 160°, because the average energy loss contributed fully to the peak width. The spectrometer was directly connected to the target in vacuum, so that resolution was not degraded by a vacuum window.

The magnetic field in the spectrometer was measured both by a precision nuclear magnetic resonance (NMR) device and a Rawson-type rotating coil gaussmeter. The

long-term stability of the spectrometer field was better than 10^{-5}. In order to reduce the background accidental rate, the spectrometer focal plane was shielded by 1.4 m of concrete and 30 cm of iron. The waste beam from the target passed through a 60 cm diam vacuum pipe to a shielded beam dump approximately 40 m downstream. An air-core magnet deflected the waste beam about 3° downward at a position 10 m from the dump to reduce back streaming of electrons toward the target.

Experimental data were acquired on line by a dedicated

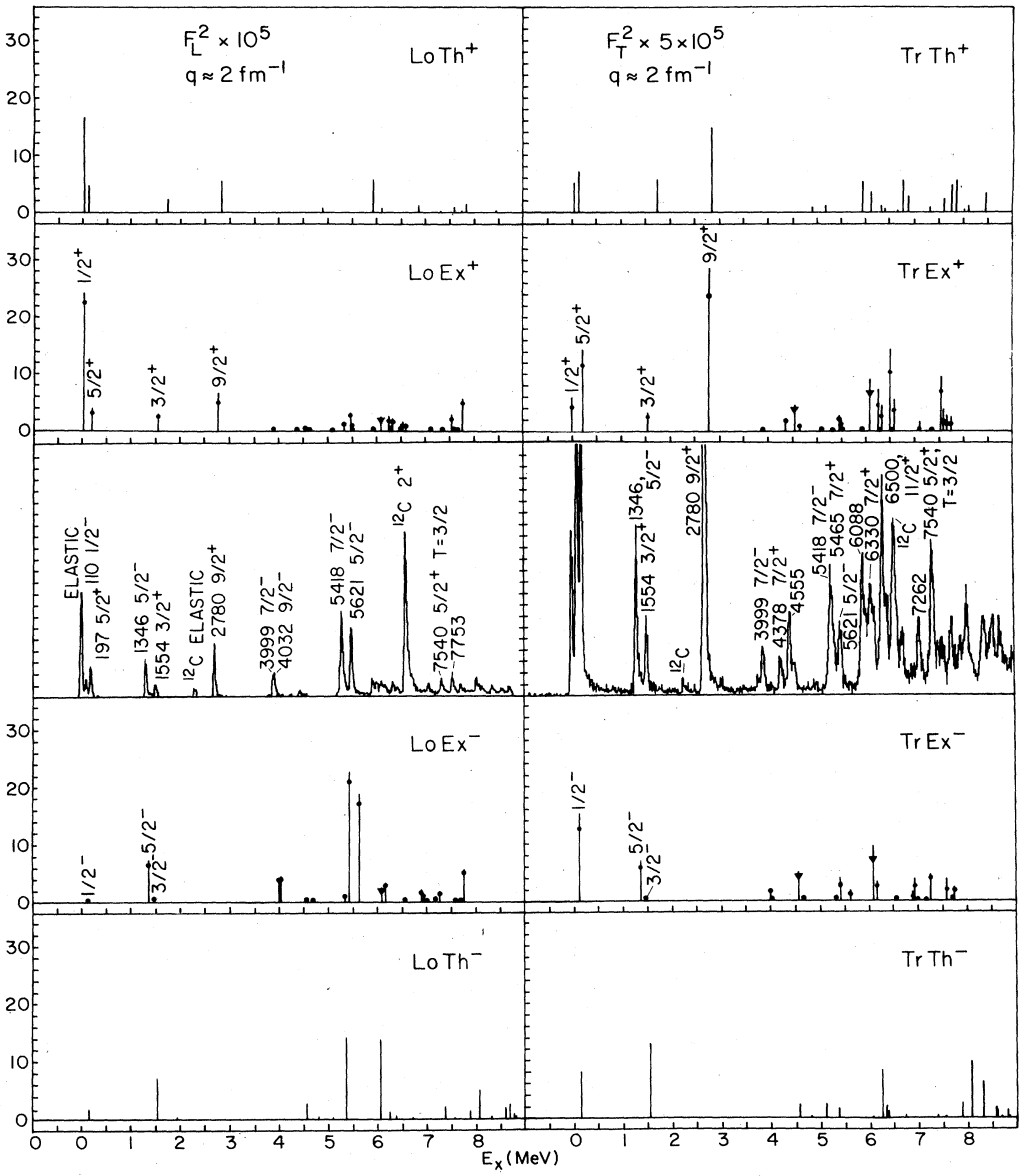

FIG. 1. Electroexcitation spectra of ^{19}F at $q = 1.95\ fm^{-1}$. The two center panels show the raw experimental spectra acquired at 271 MeV and 90° (left panel) and 194 MeV and 160° (right panel). The momentum transfers for these two spectra are approximately the same. The peaks at 2.4 and 6.8 MeV in these spectra arise from elastic and inelastic scattering on ^{12}C in the target. The 90° spectrum emphasizes the longitudinal component of the scattering and the 160° spectrum the transverse component. The panels labeled $LoEx^+$, $TrEx^+$, appearing above the center panels, and those labeled $LoEx^-$ and $TrEx^-$, appearing below the center panels, show the results of carrying out Rosenbluth separations on the raw data for the positive-parity (+) and negative-parity (−) states, respectively, to obtain the purely longitudinal (Lo) and transverse (Tr) components of the experimental (Ex) scattering. The solid circles show the experimental values extracted for the isolated states and the extension of the vertical line above the circle indicates the upper limit of the experimental error bar. The solid triangles which appear in both the positive-parity and negative-parity panels show the experimental values for the unresolved groups of states which contain both positive-parity and negative-parity members. For a given parity these triangles thus represent an upper limit for the experimental value. The top panels, labeled $LoTh^+$ and $TrTh^+$, show the predictions for form-factor values at this momentum transfer for all the states predicted for this energy range from the SD calculation. The bottom panels, labeled $LoTh^-$ and $TrTh^-$, show the predictions for the negative-parity levels from the PSD calculation.

minicomputer with a CAMAC interface to the focal-plane detector system. The computer served both to control the data acquisition and to store the accumulated data on magnetic tape for later off-line analysis. Details of this system are given in Ref. 3.

In Fig. 1 we present spectra of the scattering of electrons from a Teflon target, measured at energy-angle combinations of 271 MeV 90° and 194 MeV 160°, respectively. Many basic features of ^{19}F are manifested in the distribution and intensity of the peaks in these spectra, the first of which is dominated by longitudinal processes and the second by transverse processes. In addition, the spectra summarize the quality of the data better than words can. The peaks at apparent excitation energies of 2375 and 6813 keV in the spectra are due to elastic and inelastic scattering from the ^{12}C in the target.

III. DATA REDUCTION

A. Energy calibrations

The accelerator energy and the spectrometer dispersion constants were determined from the Teflon data for each accelerator energy. With the excellent resolution achieved in the experimental spectra, it was possible to identify a number of peaks observed distributed across the focal plane with known levels of ^{19}F. The excitation energies of the levels of ^{19}F below 7 MeV are well known,[17] and their values were used to calibrate the position along the focal plane as a function of excitation energy in ^{19}F. Since Teflon also contains ^{12}C (and 1% ^{13}C), the kinematic shifts of the carbon levels relative to the fluorine levels gave a good measure of the accelerator energy. In some cases, additional targets of different mass were bombarded as a check on the calibration. In practice, the positions of all known peaks were used as data in a least-squares fit from which the bombarding energy and focal plane parameters were obtained. Typical uncertainties in bombarding energy which resulted from using these techniques were ± 0.2 MeV.

B. Spectrum sorting and line-shape fitting

After the bombarding energy and the parameters of the focal plane were determined, these quantities were fed to a sorting program which rehistogrammed the raw spectrum into excitation energy bins of preselected width. The excitation energies of the peaks in this sorted spectrum normally matched the previously assigned energies of the levels to within ± 5 keV.

The sorted spectrum was then fed to a line-shape fitting program to extract the absolute area under each peak. Due to the low mass of the electron, it radiates freely when passing through matter. This results in a line shape which has a sharp peak, whose width is determined by instrumental resolution and target thickness, combined with a radiative "tail" that extends to lower scattered electron energies. This line shape has been derived analytically in Born approximation,[18] but the formulas are too cumbersome to use in fitting a spectrum that may have 50 or more peaks.

It has been found empirically[19] that the line shape for a sharp state can be well represented by a deformed Gaussian which is smoothly joined (continuous through first derivative) to an inverse third-order polynomial on the high-excitation energy side of the peak. In principle, eight parameters are thus needed to define each peak. In practice, it was found that the peak shape was fairly stable over the 5% useful range of the focal plane. This made it possible to determine the five parameters which define the deformation of the Gaussian and the shape of the tail by fitting to a strong representative peak and then using the same values for most of the remaining peaks.

Since many level energies of ^{19}F are well known, the positions of most of the peaks could be locked to the energies of known levels. The widths of the peaks were almost constant across the usable part of the focal surface when the spectrometer was properly tuned. Thus, for most of the peaks in the spectrum it was necessary to fit only the height of the peak, and the number of parameters to be fitted did not greatly exceed the number of peaks in the spectrum. The presently used line-shape fitting program will accommodate a spectrum with 75 peaks and 100 free parameters.

Since the line shape is semiempirical, there is no guarantee that it will have the correct form of the radiative tail upon completion of the fitting. This was checked by cutting off the integration of each peak area at five different energies greater than the excitation energy of the level in question. At each cutoff energy, a radiative correction[20,21] was calculated and multiplied into the integrated area. To be acceptable, all five corrected areas were required to agree to $\pm 2\%$. In the present experiment, cutoff energies of 0.5, 1.0, 1.5, 2.0, and 3.0 MeV above the peak excitation energy were used, and the initial parameters and/or constraints were varied until the consistency criterion was met.

For the forward angles, where transmission geometry was used, the basic line shape was dominated by instrumental resolution, since the mean spread of the straggling was two to three times smaller than the instrumental line width. At backward angles, however, detected electrons could lose any fraction of twice the full energy loss due to passage through the target. This resulted in an approximately rectangular energy spread folded into the instrumental resolution. For the targets used in this experiment, the width of this energy-loss distribution was equal to or greater than the instrumental resolution at a scattering angle of 160°.

Since the energy-loss distribution depends upon the thickness and uniformity of the target and the present experiment used several different targets, the line shape at 160° was not the same throughout the experiment. The fit of the semiempirical line shape to the actual line shapes observed at 160° was not as good as was obtained for the forward angle data. As a result, closely spaced levels could not be separated as reliably at 160° as at forward angles.

C. Determination of experimental longitudinal and transverse form factors and their errors

The values we quote for the experimental form factors for ^{19}F are based on the ratios of the counts in the ^{19}F

peaks in the spectra to those in the carbon elastic peak and on the assumption that we know the carbon values absolutely. The separation of the data into purely longitudinal and purely transverse components is made with the conventional Rosenbluth separation technique.[22]

The quoted values of the experimental errors in this work are compounded from the statistical errors extracted from the error matrices of the least-squares fits to the peak spectra and the systematic errors which result from the absolute uncertainties in the cross sections for electron scattering on ^{12}C which were used as the normalization for the ^{19}F cross sections. The statistical errors include both the diagonal (uncorrelated) and off-diagonal (correlated) elements of the error matrix.

The ^{12}C cross sections for elastic electron scattering were calculated with DWBA phase-shift analysis using the charge distribution derived by Friar and Negele[23] from experimental data on ^{12}C. An absolute uncertainty of $\pm 5\%$ was assigned to these calculations as an estimate of the systematic error. The normalization factors obtained by comparing the ^{19}F peaks to the ^{12}C elastic peak typically had values of 1.1—1.3 relative to the ^{19}F cross sections calculated from the nominal experimental parameters of integrated charge, spectrograph aperture, and target thickness. This range of deviation seems reasonable in the context of the susceptibility of the Teflon targets to physical deterioration in the electron beam.

The procedure by which the Rosenbluth separations are carried out requires the use of data from at least two different angles. These data must be considered as resulting from two or more independent measurements, since in general they derive from different targets and experimental conditions. Therefore, the total errors for the datum at each angle must include both the statistical and systematic errors. These total errors were evaluated by adding in quadrature the statistical error of the fit to the ^{12}C elastic peak with the $\pm 5\%$ systematic error. This normalization error was then added in quadrature with the statistical errors of the fits to the individual inelastic peaks to obtain the individual total errors. These errors for the data at the forward and backward angles were then propagated through the Rosenbluth separations and the resulting values are those quoted for the longitudinal and transverse form factors data.

Because of the large numbers of tables involved, the tabulations of analyzed data could not be reproduced in this paper. However, workers wishing to obtain tables of the experimental transverse and longitudinal cross sections as well as the unseparated data may do so by writing to Mr. William Lobar, Bates Linear Accelerator Center, P.O. Box 842, Middleton, MA 01949-2842.

IV. THEORETICAL FORMULATION OF ELECTRON SCATTERING FORM FACTORS IN TERMS OF MULTIPARTICLE SHELL-MODEL WAVE FUNCTIONS

A. Electron scattering cross sections in terms of form factors

The differential cross section in the one-photon exchange approximation for the scattering of an electron with initial total energy E_i and final total energy E_f from a nucleus of mass M and charge Z through an angle θ is given (see, for example, Refs. 24, 25, 22, and 26) by

$$\frac{d\sigma}{d\Omega}=\sigma(\text{Mott})\eta\sum_L\{\epsilon^2F^2(CL,q,f,i)+[(\tfrac{1}{2})\epsilon+\tan^2(\theta/2)]\times[F^2(ML,q,f,i)+F^2(EL,q,f,i)]\} \tag{1}$$

where

$$\sigma(\text{Mott})=[Z\alpha\cos(\theta/2)/2E_i\sin^2(\theta/2)]^2 ,$$

$$\eta=[1+(2E_i/M)\sin^2(\theta/2)]^{-1} ,$$

$$\epsilon=(q_u/q)^2 ,$$

$$(q_u)^2=q^2-\omega^2 ,$$

$$q^2=4E_iE_f\sin^2(\theta/2)+\omega^2 ,$$

$$\omega=E_i-E_f ;$$

q and ω are the three-momentum transfer and energy loss, respectively. The quantity α is the fine structure constant $e^2/\hbar c$. Usually η and ϵ are close to unity.

The nuclear form factors for inelastic scattering between an initial (i) and final (f) state or for elastic scattering ($i=f$) for a given multipolarity L are denoted by the longitudinal electric, or Coulomb, form factor $F(CL,q,f,i)$, the transverse magnetic form factor $F(ML,q,f,i)$, and the transverse electric form factor $F(EL,q,f,i)$. The transverse form factors can be divided into the components Lc and Lm arising from the convection currents (due to the orbital motion of the nucleons) and the magnetization currents (due to the intrinsic magnetic moments of the nucleons), respectively:

$$F(EL,q,f,i)=F(Elc,q,f,i)+F(ELm,q,f,i) , \tag{2}$$

$$F(ML,q,f,i)=F(MLc,q,f,i)+F(MLm,q,f,i) . \tag{3}$$

The indices i and f stand for all quantum numbers that are needed to specify uniquely the initial and final nuclear states. (The form factors defined in Ref. 26, F_{DW}, are related to the expressions F of Eq. (1) by $F=[(4\pi)^{1/2}/Z]F_{\text{DW}}$. With this normalization, $F(C0,q=0,\text{elastic})=1$.)

As the first step in formulating theoretical expressions for the form factors F we present results obtained for model wave functions consisting of the spherical single-particle states $|n,l,j\rangle$ of the nuclear shell model. The "single-particle" form factors corresponding to a transition from an initial single-particle state j' to a final single-particle state j are denoted by $w(q,j,j')$. In the second step, these single-particle terms for all the orbit pairs of the multiparticle shell-model basis space are weighted by the multiparticle transition amplitudes from a configuration-mixing shell-model calculation. These are added to obtain the "multiparticle" form factors $W(q,f,i)$ for a transition between the initial (i) and final (f) nuclear state. Finally, these multiparticle form factors $W(q,f,i)$ will be combined with the statistical m-substate factors and corrections for center-of-mass motion and nucleon finite size to obtain the form factors $F(q,f,i)$ of Eq. (1).

B. Form factors of the single-particle states of the shell model

The single-particle wave functions $|j,t_z\rangle$ are specified by

$$|j,t_z\rangle = |n,l,j,m,t_z\rangle = R(r,j,t_z)|j) = R(r,j,t_z)[Y^{(l)}(\hat{\mathbf{r}})\otimes\psi]^j_m\chi(t_z) , \quad (4)$$

where ψ is the spin wave function and χ is the isospin wave function. The normalization of the radial wave function $R(r,j,t_z)$ is given by

$$\int R(r,j,t_z)^2 r^2 dr = 1 . \quad (5)$$

The reduced matrix element convention used in this paper is that of Edmonds[27] and de-Shalit and Talmi.[28]

The single-particle form factors $w(q,j,j',t_z)$ are given by integrals of the appropriate multipole operators[24,25,22,26]

$$w(CL,q,j,j',t_z) = \int \langle j,t_z||Y^{(L)}(\hat{\mathbf{r}})j_L(qr)\rho(r,t_z)||j',t_z\rangle d^3r , \quad (6)$$

$$w(MLc,q,j,j',t_z) = \int \langle j,t_z||\mathbf{M}(L,L,q,\mathbf{r})\cdot\mathbf{J}(c,\mathbf{r},t_z)||j',t_z\rangle d^3r , \quad (7)$$

$$w(MLm,q,j,j',t_z) = \int \langle j,t_z||\mathbf{M}(L,L,q,\mathbf{r})\cdot\mathbf{J}(m,\mathbf{r},t_z)||j',t_z\rangle d^3r , \quad (8)$$

$$w(ELc,q,j,j',t_z) = (1/q)\int \langle j,t_z||[\nabla\times\mathbf{M}(L,L,q,\mathbf{r})]\cdot\mathbf{J}(c,\mathbf{r},t_z)||j',t_z\rangle d^3r , \quad (9)$$

$$w(ELm,q,j,j',t_z) = (1/q)\int \langle j,t_z||[\nabla\times\mathbf{M}(L,L,q,\mathbf{r})]\cdot\mathbf{J}(m,\mathbf{r},t_z)||j',t_z\rangle d^3r . \quad (10)$$

The integrals $\langle\ \rangle$ are over the nucleon coordinates r_k. In these equations $\rho(r)$ is the charge density operator, $\mathbf{J}(c,\mathbf{r})$ is the convection current density operator, and $\mathbf{J}(m,\mathbf{r})$ is the magnetic current density operator

$$\rho(r,t_z) = \sum_k P_k(t_z)g_l(t_z)e\delta(r-r_k) , \quad (11)$$

$$\mathbf{J}(c,\mathbf{r},t_z) = \sum_k P_k(t_z)g_l(t_z)u_N(-i)[\nabla_k\delta(r-r_k) + \delta(r-r_k)\nabla_k] , \quad (12)$$

$$\mathbf{J}(m,\mathbf{r},t_z) = \sum_k P_k(t_z)g_s(t_z)u_N[\nabla\times(\sigma_k/2)]\delta(r-r_k) . \quad (13)$$

In these expressions, $P(t_z)$ is the projection operator for protons ($t_z=+\frac{1}{2}$) and neutrons ($t_z=-\frac{1}{2}$), e.g., $P(\mathrm{p})|\mathrm{p}\rangle=1$ and $P(\mathrm{p})|\mathrm{n}\rangle=0$. The quantities g_l and g_s are the free nucleon g factors [$g_l(\mathrm{p})=1$, $g_l(\mathrm{n})=0$, $g_s(\mathrm{p})=5.586$, and $g_s(\mathrm{n})=-3.826$]. The nuclear magniton is denoted by $u_N=e\hbar/2m_pc=0.1051$ e fm. When the matrix elements of Eq. (12) are evaluated, the left- and right-hand side ∇ operators operate on the wave functions to the left- and right-hand sides, respectively. The ∇ operator inside the brackets [ ] of Eqs. (9) and (10) act only on $\mathbf{M}(L,L',q,\mathbf{r})$. These $\mathbf{M}$ terms are the products of spherical Bessel functions and vector spherical harmonics[29] $Y^{(L,L')}(\hat{\mathbf{r}})$:

$$\mathbf{M}(L,L',q,\mathbf{r}) = j_{L'}(qr)Y^{(L,L')}(\hat{\mathbf{r}}) . \quad (14)$$

The "angular" matrix elements of Eqs. (7)—(10) can be evaluated in terms of nine-j symbols. They are given in this form in most references.[24–26,22,30] These matrix elements can be expressed still more compactly by making use of the properties of the spherical Bessel functions and the nine-j symbols.[31,32] More details of the derivations of the expressions for the transverse magnetic form factor are given in Appendix A. The corresponding results for the longitudinal and transverse electric form factors have been given by Donnelly and Haxton.[32] The relationship between our notations and those of Donnelly and Haxton are given in Appendix B.

C. Single-particle form factors $w(q,j,j')$ in terms of single-particle transition densities $h(r,j,j')$

All five of the single-particle form factors of Eqs. (6)—(10) can be reformulated into a concise and uniform notation consisting of integrals over the radial coordinate of spherical Bessel functions $j_L(qr)$ multiplied by single-particle transition densities $h(r,j,j')$:

$$w(CL,q,j,j',t_z) = g_l(t_z)e\int h(CL,r,j,j',t_z)j_L(qr)r^2dr , \quad (15)$$

$$w(MLc,q,j,j',t_z) = g_l(t_z)u_N i\int h(MLc,r,j,j',t_z)j_L(qr)r^2dr , \quad (16)$$

$$w(MLm,q,j,j',t_z) = g_s(t_z)u_N i\int h(MLm,r,j,j',t_z)j_L(qr)r^2dr , \quad (17)$$

$$w(Elc,q,j,j',t_z) = g_l(t_z)u_N(1/q)\int h(ELc,r,j,j',t_z)j_L(qr)r^2dr , \quad (18)$$

$$w(ELm,q,j,j',t_z) = g_s(t_z)u_N q\int h(ELm,r,j,j',t_z)j_L(qr)r^2dr . \quad (19)$$

The key components in Eqs. (15)—(19), the single-particle transition densities $h(r,j,j')$, take the forms

$$h(CL,r,j,j',t_z)=C(EL,j,j')D(r,j,j',t_z)\ , \tag{20}$$

$$h(MLc,r,j,j',t_z)=[L(L+1)]^{1/2}C(ML,j,j')[1+B(j,j')/L][1-B(j,j')/(L+1)](1/r)D(r,j,j',t_z)\ , \tag{21}$$

$$h(MLm,r,j,j',t_z)=(\tfrac{1}{2})[L(L+1)]^{-1/2}C(ML,j,j')\{B(j,j')D'(r,j,j',t_z)+[B(j,j')-L(L+1)](1/r)D(r,j,j',t_z)\}\ , \tag{22}$$

$$h(ELc,r,j,j',t_z)=[L(L+1)]^{-1/2}C(EL,j,j')(1/r)\{L(L+1)D^{-}(r,j,j',t_z)+[l(l+1)-l'(l'+1)]D'(r,j,j',t_z)\}\ , \tag{23}$$

and

$$h(ELm,r,j,j',t_z)=(\tfrac{1}{2})[L(L+1)]^{-1/2}C(EL,j,j')[j(j+1)-j'(j'+1)-l(l+1)+l'(l'+1)]D(r,j,j',t_z)\ . \tag{24}$$

The values of the quantities B, C, and D are given by

$$B(j,j')=j(j+1)+j'(j'+1)-l(l+1)-l'(l'+1)+\tfrac{1}{2}\ , \tag{25}$$

$$C[(E/M)L,j,j']=(-1)^{j+1/2}P[(E/M)L,l,l']\begin{bmatrix} j & L & j' \\ \frac{1}{2} & 0 & -\frac{1}{2}\end{bmatrix}[(2j+1)(2L+1)(2j'+1)/4\pi]^{1/2}\ , \tag{26}$$

where

$$P(EL,l,l')=[1+(-1)^{l+l'+L}]/2\ , \tag{27}$$

$$P(ML,l,l')=[1+(-1)^{l+l'+L+1}]/2\ , \tag{28}$$

and

$$D(R,j,j',t_z)=R(r,j,t_z)R(r,j',t_z)\ , \tag{29}$$

$$D'(r,j,j',t_z)=R(r,j,t_z)R'(r,j',t_z)+R'(r,j,t_z)R(r,j',t_z)\ , \tag{30}$$

$$D^{-}(r,j,j',t_z)=R(r,j,t_z)R'(r,j',t_z)-R'(r,j,t_z)R(r,j',t_z)\ , \tag{31}$$

where R' is the derivative of the radial wave function R. We note that $C(EL,j,j')$ is the reduced matrix element of $Y^{(L)}$ as given by de-Shalit and Talmi.[28] $C[(E/M)L,j,j']$ has the property that under interchange of j and j',

$$C(L,j',j)=(-1)^{j'-j}C(L,j,j')\ . \tag{32}$$

Hence the functions $h(r)$ have the properties

$$h(Cl,r,j',j,t_z)=(-1)^{j'-j}\,h(CL,r,j,j',t_z)\ , \tag{33}$$

$$h(ML,r,j',j,t_z)=(-1)^{j'-j}\,h(ML,r,j,j',t_z)\ , \tag{34}$$

$$h(EL,r,j',j,t_z)=-(-1)^{j'-j}\,h(EL,r,j,j',t_z)\ . \tag{35}$$

D. Multiparticle form factors $W(q,f,i)$ and transition densities $H(r,f,i)$

The reduced matrix element of a one-body tensor operator $O^{(L)}$ between multiparticle states can be expressed as a sum of the products of the elements of multiparticle transition amplitudes (A) times single-particle matrix elements, where the sum runs over all pairs of single-particle states in the model space.[33]

$$\langle f,T_Z||O^{(L)}(t_z)||i,T_Z\rangle=\sum_{j,j'}A(L,j,j',f,i,T_Z,t_z)\langle j,t_z||O^{(L)}||j',t_z\rangle\ . \tag{36}$$

The multiparticle transition amplitudes are defined as

$$A(L,j,j',f,i,T_Z,t_z)=(2L+1)^{-1/2}\langle f,T_z||[a^{\dagger}(j,t_z)\otimes\tilde{a}(j',t_z)]^{(L)}||i,T_Z\rangle\ , \tag{37}$$

where $a^{\dagger}$ and $\tilde{a}$ are the nucleon creation and destruction operators. The relationship between the multiparticle amplitudes in isospin and proton-neutron formalism is given in Appendix C.

In this context, multiparticle transition between densities (H) and multiparticle form factors (W) are given by

$$H(XL,r,f,i,T_Z,t_z)=\sum_{j,j'}A(L,j,j',f,i,T_Z,t_z)h(XL,r,j,j',t_z)\ , \tag{38}$$

$$W(XL,q,f,i,T_Z,t_z)=\sum_{j,j'}A(L,j,j',f,i,T_Z,t_z)w(XL,q,j,j',t_z)\ , \tag{39}$$

where "X" stands for C, Mc, Mm, Ec, or Em.

E. Relationship between $W(ELc)$ and $W(CL)$ provided by the continuity equation

The charge density operator and the charge current operator are related by the continuity equation

$$(d/dt)\rho(\mathbf{r},t_z)=-\nabla\cdot\mathbf{J}(\mathbf{r},t_z)\ . \tag{40}$$

The density and current, in general, involve the motions of the nucleons as well as the motions of the exchanged mesons which bind the nucleons together. The fact that the "exchange" densities in the $q\rightarrow 0$ limit can be neglected on the left-hand side of Eq. (40) is known as Seigert's theorem[34] and is a generalization of the idea of charge conservation. However, at this same level of approximation the exchange current cannot be neglected and hence the total current on the right-hand side should be the sum of the convection current $\mathbf{J}(c)$ and exchange current $\mathbf{J}(e)$.

Some insight into the role of the exchange current can be obtained by considering the commutator of the total Hamiltonian $H=T+V$ with the density operator

$$(d/dt)\rho(\mathbf{r},t_z)=(i/\hbar)[H,\rho(\mathbf{r},t_z)]=(i/\hbar)[T,\rho(\mathbf{r},t_z)]+(i/\hbar)[V,\rho(\mathbf{r},t_z)]\ , \tag{41}$$

with

$$(i/\hbar)[T,\rho(\mathbf{r},t_z)]=-\nabla\cdot\mathbf{J}(c,\mathbf{r},t_z) \tag{42}$$

and

$$(i/\hbar)[V,\rho(\mathbf{r},t_z)]=-\nabla\cdot\mathbf{J}(e,\mathbf{r},t_z)\ . \tag{43}$$

Thus, the exchange currents arise from the components of the interaction V, such as momentum-dependent components, which do not commute with the density operator in Eq. (43).

For bound states with binding energies E_b, the matrix element of the left-hand side of Eq. (40) is given simply by

$$\langle f\,|\,(d/dt)\rho(\mathbf{r},t_z)\,|\,i\rangle = (i/\hbar)(E_{bf}-E_{bi})\langle f\,|\,\rho(\mathbf{r},t_z)\,|\,i\rangle\ . \tag{44}$$

The contribution of the exchange current is thus taken into account by the binding energy difference which appears on the right-hand side of Eq. (44). It is much easier to evaluate the right-hand of Eq. (44) than to evaluate the matrix element of the exchange current directly. Thus, if a way can be found to make use of Eqs. (40) and (44), the contribution of the exchange current can be more easily taken into account.

The standard method[35,36] of introducing the continuity equation into the reduction of the transverse ELc matrix element [Eq. (9)], while not unique,[37] is to integrate Eq. (9) by parts to obtain the single-particle form factor in the form

$$w(ELc,q,j,j',t_\cdot)=w(ELc_1,q,j,j',t_z)+w(ELc_2,q,j,j',t_z)\ , \tag{45}$$

where

$$w(ELc_1,q,j,j',t_z)=(i/q)[L(L+1)]^{-1/2}\int\langle j,t_z||j_L(qr)Y^{(L)}[(\mathbf{r}\cdot\nabla+2)\nabla\cdot\mathbf{J}(c,\mathbf{r},t_z)]||j',t_z\rangle d^3r \tag{46}$$

and

$$w(ELc_2,q,j,j',t_z)=-(i/q)[L(L+1)]^{-1/2}\int\langle j,t_z||j_L(qr)Y^{(L)}\{\nabla^2[\mathbf{r}\cdot\mathbf{J}(c,\mathbf{r},t_z)]\}||j',t_z\rangle d^3r\ . \tag{47}$$

Using the continuity equation, the term $\nabla\cdot\mathbf{J}$ in Eq. (46) can be replaced by $-(d/dt)\rho$. The single-particle form factor of Eq. (46) can then be expressed in the form

$$w(ELc_1,q,j,j',t_z)=g_l(t_z)(e/\hbar c)[\epsilon(j)-\epsilon(j')](1/q)\int h(ELc_1,r,j,j',t_z)j_L(qr)r^2dr \tag{48}$$

with

$$h(ELc_1,r,j,j',t_z)=[L(L+1)]^{-1/2}[2h(CL,r,j,j',t_z)+r\,dh(CL,r,j,j',t_z)/dr]\ , \tag{49}$$

where $\epsilon(j)$ are the single-particle energies.

Evaluation of Eq. (47) gives

$$w(Elc_2,q,j,j',t_z)=g_l(t_z)u_N q\int h(ELc_2,r,j,j',t_z)j_L(qr)r^2dr \tag{50}$$

with

$$h(ELc_2,r,j,j',t_z)=[L(L+1)]^{-1/2}C(EL,j,j')rD^-(r,j,j',t_z)\ . \tag{51}$$

Since the continuity equation cannot be employed for the term ELc_2, the exchange-current contribution must be added explicitly for this term. In this paper this exchange-current contribution is ignored.

In the case of multiparticle states, the relation between the longitudinal and transverse form factors provided by the continuity equation should apply to the total Hamiltonian, and Eq. (48) becomes

$$W(ELc_1,q,f,i,T_Z,t_z)=g_l(t_z)(e/\hbar c)(E_{bf}-E_{bi})(1/q)\int H(ELc_1,r,f,i,T_Z,t_z)j_L(qr)r^2dr \tag{52}$$

with

$$H(ELc_1,r,f,i,T_Z,t_z)=[L(L+1)]^{-1/2}[2H(CL,r,f,i,T_Z,t_z)+r\,dH(CL,r,f,i,T_Z,t_z)/dr]\ , \tag{53}$$

where E_{bi} and E_{bf} are the total binding energies of the initial and final states, respectively.

F. Corrections to the point-nucleon form factors

Several corrections must be applied to the point-nucleon form factors of Eq. (39) to convert them into a representation appropriate for comparison with experimental form factors. These corrections are accomplished by multiplying the expressions W of Eq. (39) by a statistical factor, an overall normalization, and by form factors corresponding to corrections for center-of-mass motion and the finite size of the nucleons. This produces the nuclear form factors F in Eq. (1),

$$F(XL,q,f,i)=(2J_i+1)^{-1/2}[(4\pi)^{1/2}/Z]G_{\text{c.m.}}(q)\times\sum_{t_z}[W(XL,q,f,i,T_Z,t_z)/g(X,t_z)]g_{fs}(X,q,t_z)\ . \tag{54}$$

The factor $(2J_i+1)^{-1/2}$ arises on going from the reduced matrix element to the matrix element summed over final m substates and averaged over initial m substates. The normalization $(4\pi)^{1/2}/Z$ is chosen to make $F(C0,q=0,\text{elastic})=1$, as noted above. The term $G_{\text{c.m.}}$ is the center-of-mass correction. It divides out the form factor due to the spurious motion of the center of mass which is inherent in the fixed-center shell-model formulation. The conventional harmonic-oscillator approximation for this correction is used in this work. In this approximation the center of mass is assumed to be in a $0s$ state.[38,22] This gives

$$G_{\text{c.m.}}(q)=\exp(b^2q^2/4A)\ , \tag{55}$$

where b is the oscillator length parameter chosen to reproduce the rms radius of the nucleus.

To take into account the finite size of the nucleons we start by dividing by the free nucleon g factors at $q=0$, denoted in Eq. (54) by

$$g(Mc,t_z)=g(Ec,t_z)=g(C,t_z)=g_l(t_z)$$

and

$$g(Mm,t_z)=g(Em,t_z)=g_s(t_z)\ .$$

[Note that these cancel the original "g factors" which appear in Eqs. (15)–(19)]. Then we multiply by the equivalent q-dependent form factors for free nucleons,[22]

$$g_{fs}(Mc,q,t_z)=g_{fs}(Ec,q,t_z)=g_{fs}(C,q,t_z)=g(c,q,t_z)$$

and

$$g_{fs}(Mm,q,t_z)=g_{fs}(Em,q,t_z)=g(m,q,t_z)\ . \tag{56}$$

These are normalized so that

$$g_{fs}(X,q=0,t_z)=g(X,t_z)\ .$$

Three quantities $g_{fs}(c,q,\text{p})$, $g_{fs}(c,q,\text{n})$, and $g_{fs}(m,q,\text{p})$ are well determined experimentally,[39] and we use the conventional approximation

$$g_{fs}(m,q,\text{n})/g_s(\text{n})=g_{fs}(m,q,\text{p})/g_s(\text{p})$$

for the fourth.

For most purposes the longitudinal form factor can be approximated in terms of just the point-proton form factor, by

$$\begin{aligned}F(CL,q,f,i)=&(2J_i+1)^{-1/2}[(4\pi)^{1/2}/Z]G_{\text{c.m.}}(q)\\&\times[g_{fs}(c,q,\text{p})+(N/Z)g_{fs}(c,q,\text{n})]\\&\times W(CL,q,f,i,T_Z,\text{p})\ .\end{aligned} \tag{57}$$

G. Gamma-decay transition probabilities and electromagnetic moments

The standard gamma-decay transition matrix elements $M(EL)$ and $M(ML)$, as defined for example in Ref. 33, are related to the form factors $F(EL)$ and $F(ML)$, respectively, in the limit at which $\hbar c$ times the momentum transfer is equal to the transition energy $E_\gamma=E_{bf}-E_{bi}$. For small q we can use $G_{\text{c.m.}}(q\to0)=1$ and $g(t_z)/g_{fs}(q\to0,t_z)=1$ in Eq. (54) to obtain the relationship in terms of $W(EL)$ and $W(ML)$

$$\begin{aligned}M(EL)&=\lim_{q\to E_\gamma/\hbar c}\frac{(2J_i+1)^{1/2}(2L+1)!!Z[L/(L+1)]^{1/2}F(EL,q)}{q^L(4\pi)^{1/2}}\\&=\lim_{q\to E_\gamma/\hbar c}q^{-L}(2L+1)!![L/(L+1)]^{1/2}\sum_{t_z}W(EL,q,t_z)\ ,\end{aligned} \tag{58}$$

$$\begin{aligned}M(ML)&=\lim_{q\to E_\gamma/\hbar c}\frac{(2J_i+1)^{1/2}(2L+1)!!Z[L/(L+1)]^{1/2}F(ML,q)}{iq^L(4\pi)^{1/2}}\\&=\lim_{q\to E_\gamma/\hbar c}-iq^{-L}(2L+1)!![L/(L+1)]^{1/2}\sum_{t_z}W(ML,q,t_z)\ .\end{aligned} \tag{59}$$

As $q\to E_\gamma/\hbar c$ there is a unique relationship between $W(EL)$ and $W(CL)$ provided by the continuity equation. Using the results of Sec. IV E, with $j_L(qr)\to(qr)^L/(2L+1)!!$, the term $W(ELc_2)$ can be neglected relative to $W(ELc_1)$ in Eq. (45) and, integrating the derivative term in Eq. (53) by parts, one obtains

$$\begin{aligned}W(ELc,q\to E_\gamma/\hbar c,f,i,T_Z,t_z)&=W(ELc_1,q\to E_\gamma/\hbar c,f,i,T_Z,t_z)\\&=g_l(t_z)eq^L\int H(ELc_1,r,f,i,T_Z,t_z)r^Lr^2dr/(2L+1)!!\\&=-g_l(t_z)e[(L+1)/L]^{1/2}q^L\int H(CL,r,f,i,T_Z,t_z)r^Lr^2dr/(2L+1)!!\\&=-[(L+1)/L]^{1/2}W(CL,q\to E_\gamma/\hbar c,f,i,T_Z,t_z)\ .\end{aligned} \tag{60}$$

This relationship is valid for the total nucleon plus exchange current contribution and not generally for the nucleon contribution alone. Since the exchange current contribution to $W(CL)$ is small compared to the corresponding correction for $W(EL)$ (see Sec. IV E), it is preferable to use Eq. (60) rather than $W(EL)$ directly, which gives

$$M(EL)=-\lim_{q\to E_\gamma/\hbar c}q^{-L}(2L+1)!!\sum_{t_z}W(CL,q,t_z)\ . \tag{61}$$

From Eqs. (15), (39), and (54), the $M(EL)$ matrix element can be obtained explicitly as

$$M(EL,f,i,T_Z)=-e\sum_{t_z} g_l(t_z)\int H(CL,r,f,i,T_Z,t_z)r^L r^2 dr$$
$$=-e\sum_{j,j'}\sum_{t_z} g_l(t_z)A(L,j,j',f,i,T_Z,p)C(EL,j,j')\int D(r,j,j',t_z)r^L r^2 dr\ . \tag{62}$$

From Eqs. (3), (16), (17), (39), (54), and those given in Appendix A, the $M(ML)$ matrix element can be obtained explicitly as

$$M(ML,f,i,T_Z)=u_N[L/(L+1)]^{1/2}\sum_{t_z}\left[g_l(t_z)\int H(MLc,r,f,i,T_Z,t_z)r^L r^2 dr+g_s(t_z)\int H(MLm,r,f,i,T_Z,t_z)r^L r^2 dr\right]$$
$$=u_N(2L+1)[L/(L+1)]^{1/2}\sum_{t_z}\left[g_l(t_z)\int H(MLc^-,r,f,i,T_Z,t_z)r^{L-1}r^2 dr\right.$$
$$\left.+g_s(t_z)\int H(MLm^-,r,f,i,T_Z,t_z)r^{L-1}r^2 dr\right]$$
$$=u_N\sum_{j,j'}\sum_{t_z}A(L,j,j',f,i,T_Z,t_z)C(ML,j,j')$$
$$\times\{g_l(t_z)L[1+B(j,j')/L][1-B(j,j')/(L+1)]$$
$$-g_s(t_z)(L/2)[1+B(j,j')/L]\}\int D(r,j,j',t_z)r^{L-1}r^2 dr\ .$$

In terms of these matrix elements, the gamma transition probabilities are given by

$$B(EL)=M(EL)^2/(2J_i+1)$$

and

$$B(ML)=M(ML)^2/(2J_i+1) \tag{63}$$

and the electromagnetic moments are given by

$$m[(E/M)L]=\begin{bmatrix} J & L & J \\ -J & 0 & J \end{bmatrix}[4\pi/(2L+1)]^{1/2}$$
$$\times M[(E/M)L]\ . \tag{64}$$

The conventional notations[40] are $\mu=m(M1)$ for the magnetic dipole moment, $Q=2m(E2)$ for the electric quadrupole moment, $\Omega=-m(M3)$ for the magnetic octupole moment, $Q_4=m(E4)$ for the electric hexadecapole moment, and $\Gamma=m(M5)$ for the magnetic triakontadupole moment.

V. SHELL-MODEL FORMULATIONS OF ^{19}F WAVE FUNCTIONS

A. Model space and Hamiltonian assumptions

For the positive-parity levels of ^{19}F, the calculations from which we obtain wave functions, values of the $A(L,j,j')$ and, hence, form factor predictions for comparison with the present experimental data, are carried out in the full space of *sd*-shell configurations for the three active particles. The Hamiltonian we use, which governs the configuration mixing within this space, is a new mass-dependent *sd*-shell (MDSD) interaction which has been fixed from a fit to energy levels of all *sd*-shell nuclei.[41] The predictions for ^{19}F thus reflect the synthesis of orthodox *sd*-shell behavior as it is sampled over the entire $A=17$–39 region, projected into the three-particle system. There is hence little leeway for these calculations to be influenced by the local peculiarities associated with favored particle-hole excitations which break the ^{16}O closed-shell core. The theoretical results should thus give us the empirical picture of the "pure" *sd*-shell structure of ^{19}F. We refer to these results as the "SD" predictions.

For negative-parity levels of ^{19}F we compare the present data with predictions from calculations which use the full space of *sd*-shell configurations for four active particles coupled onto one hole in either the $p_{1/2}$ or the $p_{3/2}$ orbital. These calculations use the particle-hole Hamiltonian of Millener and Kurath, which was chosen to give a good account of the non-normal parity states in a number of nuclei from ^{11}Be to ^{16}O.[42] For the "particle-particle" interaction in these calculations we have used the Preedom-Wildenthal (PW) *sd*-shell Hamiltonian[43] and for the "hole-hole" interaction, the Cohen-Kurath *p*-shell Hamiltonian.[44] We will refer to these results as the "PSD" predictions.

It would have been more consistent to use in the PSD calculations the *sd*-shell Hamiltonian we use for the SD calculations, rather than the PW particle-particle Hamiltonian. However, for ^{19}F there is very little difference between the results obtained with the PW interaction and the new MDSD interaction. The spurious states which arise in this space were removed using the method of Gloeckner and Lawson.[45]

The excitation energies of the intruder states of the type $(p)^{(-m)}(sd)^{(3+m)}$ for $m=2$, 3, and 4 have been estimated from calculations in the full $(p_{1/2},d_{5/2},s_{1/2})$ model space which use the interaction of Reehal and Wildenthal.[46]

These results will be referred to as the Zuker, Buck, and McGrory (ZBM) (Refs. 47 and 48) model-space predictions. We will not present comparisons of experiment with the form factors calculated in the ZBM model space because the ZBM wave functions are in some aspects intrinsically inferior to those obtained in the SD and PSD model spaces. This is because of the absence of the coherent contributions of the $p_{3/2}$ with the $p_{1/2}$ and of the $d_{3/2}$ with the $d_{5/2}$ orbitals. In the future it would be interesting to make comparisons with ZBM-type wave functions which have been extended to include these other orbits.

B. Calculation of the radial wave functions and form factors

The multiparticle transition amplitudes were calculated from the SD and PSD wave functions discussed above and then combined with the single-nucleon transition densities to obtain the plane-wave electron scattering form factors as described in Sec. IV. [For the convection current part of the transverse electric form factor we use Eq. (52) which makes use of the continuity equation.] Comparisons with experiment are made by plotting the experimental form factors vs $q_{\rm eff}$ and the calculated form factors vs q. The effective momentum transfer $q_{\rm eff}$ is given by

$$q_{\rm eff}=q[1+(3Ze^2)/(2E_iR_{\rm ch})] , \tag{65}$$

where E_i is the initial total energy of the electron and $R_{\rm ch}$ is related to the rms charge radius $r_{\rm ch}$ of 2.898 fm (see below) by $R_{\rm ch}=(\frac{5}{3})^{1/2}r_{\rm ch}$. For this small Z value, the difference between PWBA vs q and DWBA vs $q_{\rm eff}$ for the inelastic scattering form factors is in general much smaller than the experimental errors and remaining theoretical uncertainties. For comparison with the more accurate longitudinal elastic scattering data, we use the DWBA form factor plotted vs $q_{\rm eff}$ obtained from the MIT elastic phase-shift code.[49]

The radial wave functions required for the single-nucleon transition densities were calculated with the harmonic-oscillator prescription. The oscillator length parameter $b=b_{\rm rms}=1.833$ fm was chosen to reproduce the rms charge radius of 2.898 ± 0.010 fm for ^{19}F obtained from muonic atom data.[50] The longitudinal elastic ($C0$) DWBA form factor calculated with this choice is compared with experiment in Fig. 3. The agreement of the calculated form factors with experiment can be made essentially perfect by adjusting the oscillator length parameter to $b=b_{\rm elastic}=1.806$ fm (see Fig. 3). The rms charge radius obtained with $b_{\rm elastic}$ is 2.813 fm, which is far outside the error bar on the muonic atomic experimental value. The origin of this discrepancy is not clear. For all remaining calculations presented here we use $b_{\rm elastic}$ to generate the radial wave functions.

C. "Effective charges" for the $C2$, $C3$, and $C4$ operators

It is well established that the $B(EL)$ values which are obtained in the SD model-space calculations, and the associated CL form factors through the first maximum, are too small by about factors of 3 ($C2$) and 4 ($C4$).[51] The primary reason for this is that the "giant resonance" excitations for the $C2$ and $C4$ operators couple coherently with the low lying states. Since these excitations involve, for example, $(0s)\rightarrow(0d\,1s)$ and $(0p)\rightarrow(0f\,2p)$ transitions, they lie outside the SD model space and must be put in by a separate calculation. This could be done microscopically using perturbation theory.[52] For the purpose of our comparisons here, it is adequate to include these admixtures by an "additive" effective charge model.[51]

The effective-charge model is usually applied just to the $B(EL)$ in terms of the model-space gamma-decay matrix elements $M^{\rm SD}(EL,t_z)$ defined in analogy with (62) by

$$\begin{aligned}M^{\rm SD}(EL,f,i,T_Z,t_z)&=-\int H^{\rm SD}(EL,r,f,i,T_Z,t_z)r^{L+2}dr\\&=-\sum_{j,j'}^{\in{\rm SD}}A(L,j,j',f,i,T_Z,t_z)C(EL,j,j')\int D(r,j,j',t_z)r^{L+2}dr ,\end{aligned} \tag{66}$$

where the superscript "SD" on M and H indicates that only the SD space multiparticle transition amplitudes are included in the summation. The total matrix element is then given in terms of these $M^{\rm SD}(EL)$ and the effective charges $\delta be(EL,t_z)$

$$M(EL,{\rm p})=M^{\rm SD}(EL,{\rm p})e+\delta M(EL,{\rm p}) \tag{67}$$

where

$$\begin{aligned}\delta M(EL,{\rm p})&=\delta e(EL,{\rm p})M^{\rm SD}(EL,{\rm p})\\&\quad+\delta e(EL,{\rm n})M^{\rm SD}(EL,{\rm n}) .\end{aligned} \tag{68}$$

(Here and below the explicit dependence of the quantities on "f,i,T_Z" is dropped.) In order to extend this formulation to the CL form factor, it is most natural to add onto the SD space transition density $H^{\rm SD}$ a collective transition density H^T which is normalized so that its gamma-decay matrix element M^T is equal to $\delta M(EL,{\rm p})$ in Eq. (67). For the giant resonance, the Tassie model[53] for the collective transition density is appropriate. Thus, we use[51]

$$H(CL,r)=H^{\rm SD}(CL,r)+H^T(CL,r) , \tag{69}$$

where $H^{\rm SD}(CL,r)$ is the point-proton transition density calculated with the SD model space multiparticle transition amplitudes and $H^T(CL,r)$ is the Tassie collective model transition density for the point protons

$$H^T(CL,r)=N_Tr^{L-1}dH[C0({\rm elastic}),r,{\rm p}]/dr . \tag{70}$$

N_T is chosen so that the gamma-decay matrix element for $H^T(CL,r)$ is equal to $\delta M(CL,{\rm p})$.

From a systematic study of $C2$ and $C4$ form factors

for even-even nuclei in the *sd* shell,[51] it has been established that the optimum empirical values for the effective charges are

$$\delta e(E2,\mathrm{p})=\delta e(E2,\mathrm{n})=0.35e \tag{71}$$

and

$$\delta e(E4,\mathrm{p})=\delta e(E4,\mathrm{n})=0.50e\ . \tag{72}$$

We have used these values for the SD model space calculations. For the PSD calculation, the $3\hbar\omega$ excitations give rise to a similar renormalization for the $C3$ operator. Our PSD comparisons have been made with

$$\delta e(E3,\mathrm{p})=\delta e(E3,\mathrm{n})=0.50e\ . \tag{73}$$

In addition, we might expect similar model-space truncation effects for the other operators; $C0$, $M1$, $E2$, $M3$, $E4$, and $M5$ in the SD space and $C1$, $E1$, $M2$, $E3$, and $M4$ in the PSD space. We have chosen to present the calculations for all of these form factors using the free-nucleon orbital and spin g factors. The comparison with experiment will then indicate, among other things, the importance of the extra-model-space configurations to these processes. [The effective charges are used in the calculation of $H(CL,r)$ which appears in Eq. (53) for the convection current part of the transverse electric operator.]

D. Center-of-mass correction for the $C1$ operator

The usual prescription for the center-of-mass correction to the form factors [Eq. (55)] applies only for the $0\hbar\omega$ (SD space) excitations, when the center of mass is in a $0s$ state. Here, we examine the additional considerations which are necessary for the $C1$ operator and the corrections corresponding to the $1\hbar\omega$ (PSD) space.

The gamma-decay $C1$ operator is particularly simple (it is just proportional to the vector radial operator), and the associated center-of-mass correction is important and straightforward to evaluate.[33] The result can be expressed in the form of Eqs. (66) and (67) with the effective charges

$$\delta e(C1,\mathrm{p})=\delta e(C1,\mathrm{n})=-Z/Ae\ . \tag{74}$$

The most naive correction which would incorporate this center-of-mass correction into the $C1$ transition density would be to subtract a term proportional to the center-of-mass radial vector. This, however, would diverge for large q. This divergence can be corrected by introducing the harmonic-oscillator exponential radial factor. We will use for the center-of-mass corrected quantity $H^{\mathrm{c.m.}}(C1,r)$

$$H^{\mathrm{c.m.}}(C1,r)=H(C1,r)+N_{\mathrm{c.m.}}\,r\exp(-r^2/b^2)\ , \tag{75}$$

where the normalization $N_{\mathrm{c.m.}}$ is chosen so that the gamma-decay matrix element for the term $N_{\mathrm{c.m.}}\,r\exp(-r^2/b^2)$ is equal to

$$(-Z/A)[M(E1,\mathrm{p})+M(E1,\mathrm{n})]e\ . \tag{76}$$

The integral of $r\exp(-r^2/b^2)$ can be evaluated analytically to obtain

$$N_{\mathrm{c.m.}}=\frac{(-Z/A)[M(E1,\mathrm{p})+M(E1,\mathrm{n})]}{(\frac{3}{8})b^5(4\pi)^{1/2}}\ . \tag{77}$$

VI. ANALYSIS OF EXPERIMENTAL AND THEORETICAL RESULTS FOR ^{19}F

We will use several different perspectives in comparing the features of ^{19}F revealed in the present electron scattering experiment with the predictions of shell-model formulations for the structure of this system. The foundation for these analyses is the summary of experimental results of energy level spectroscopy for ^{19}F compiled in Ref. 17. We assume that essentially all levels of ^{19}F which occur in the region below 8 MeV excitation energy have been identified and have been assigned their spin and parity. We present the summary of these results in Tables I and II. Together with this summary of experimental information of ^{19}F energy levels, we present in Table I the energies obtained in the three shell-model calculations considered in this study.

The associations made in Table I between experimental and model states are tentative in many cases and in a few cases arbitrary. For the lowest states of each spin and parity there is little leeway in making these associations if we are to attach any serious meaning to the model results. For the higher-lying states, however, considerable ambiguity can exist as to which experimental state best corresponds to a model state or even whether any one-to-one correspondence is meaningful. Some experimental states appear to arise from configurations which are not encompassed by any of the model spaces we consider here. Despite these problems we have, insofar as is practical, forced a one-to-one match between experimental levels and the composite of the theories in order to clarify how well our present theories reproduce the observed level density. In some cases where the experimental level density is higher than theory, we examine matches which differ from our initial one-to-one match; these are indicated in Table I by the theoretical energies in brackets. As a supplement to Table I, we present in Table II a summary of measured and predicted $B(L)$ values for the electromagnetic transitions from the ^{19}F ground state to the lowest four states of each spin and parity to which it can connect in the model spaces considered in the present work.

We see from Table I that the ZBM space with the Reehal-Wildenthal interaction produces essentially a one-to-one match with experiment up to 6.5 MeV excitation. There is likewise a good correspondence between the negative-parity levels from the ZBM model and the results of the PSD model up through 8 MeV. This indicates that states with dominant 6p-3h character tend to lie higher than 8 MeV in excitation energy. There are many more positive-parity states produced in the ZBM model calculation than in the SD space calculation. We interpret these excess states in the ZBM results as arising from configurations in which the ^{16}O core is broken. It should be remembered in the context of these remarks that the ZBM

TABLE I. Experimental and theoretical energy levels ($2J_n^\pi$ Ex) for ^{19}F.

Experiment[a] positive parity $2J_n^+$ Ex (keV)	Experiment[a] negative parity $2J_n^-$ Ex (keV)	$(sd)^3$ positive parity $2J_n^+$ Ex (keV)	ZBM positive parity $2J_n^+$ Ex (keV)	*psd* negative parity $2J_n^-$ Ex (keV)	ZBM negative parity $2J_n^-$ Ex (keV)
Levels below 8.0 MeV—matched experiment and theory					
1_1^+ 0		1_1^+ 0	1_1^+ 0		
	1_1^- 110			1_1^- 110[e]	1_1^- 240
5_1^+ 197		5_1^+ 99	5_1^+ 235		
	5_1^- 1346			5_1^- 1507	5_1^- 1419
	3_1^- 1459			3_1^- 1900	3_1^- 1702
3_1^+ 1554		3_1^+ 1698	3_1^+ 2350		
9_1^+ 2780		9_1^+ 2810	9_1^+ 2579		
3_2^+ 3908		$(3_1^+$ 1698)[c]	3_2^+ 2980		
	7_1^- 3999			7_1^- 4538	7_1^- 4386
	9_1^- 4032			9_1^- 3804	9_1^- 3992
7_1^+ 4378		$(7_1^+$ 4871)	7_1^+ 3942		
5_2^+ 4550[b]		$(5_2^+$ 5155)	5_2^+ 3801		
	3_2^- 4556[b]			3_2^- 5071	3_2^- 5164
13_1^+ 4648		13_1^+ 4798	13_1^+ 5239		
	5_2^- 4682			5_2^- 4775	5_2^- 4740
5_3^+ 5107		$(5_2^+$ 5155)	5_3^+ 5299		
$1_2^{(+)}$ 5337		$(1_2^+$ 6084)	1_2^+ 5090	$(1_2^-$ 6212)	$(1_2^-$ 6862)
	7_2^- 5418			7_2^- 5334	7_2^- 5528
7_2^+ 5464		$(7_1^+$ 4871)	7_2^+ 5738		
		$(7_2^+$ 5901)			
3_3^+ 5501		$(3_2^+$ 6627)	3_3^+ 5975		
5_4^+ 5535		5_2^+ 5155	5_4^+ 5446		
	5_3^- 5621			5_3^- 6030	5_3^- 5818
1_3^+ 5938		$(1_2^+$ 6084)	$(1_2^+$ 5090)		
7_3^+ 6070[b]		$(7_2^+$ 5901)	7_3^+ 6170		
	3_3^- 6088[b]			3_3^- 6346	3_3^- 6953
	9_2^- 6100[b]			9_2^- 5434	9_2^- 6746
	7_3^- 6161			7_3^- 6334	7_3^- 6494
1_4^+ 6255		1_2^+ 6084	1_3^+ 6216		
5_5^+ 6282		$(5_3^+$ 6373)	5_5^+ 6082		
7_4^+ 6330		7_2^+ 5901	7_4^+ 6310		
	1_2^- 6429[d]			$(1_2^-$ 6212)	$(1_2^-$ 7156)
3_4^+ 6497[b]		$(3_2^+$ 6627)	3_4^+ 6772		
11_1^+ 6500[b]		11_1^+ 6729	11_1^+ 5889		
3_5^+ 6528		3_2^+ 6627	3_5^+ 7654		
7? 6554		$(7_3^+$ 6297)	7_5^+ 7358		
9_2^+ 6592		9_2^+ 6841	9_2^+ 6386		
	3_4^- 6787			3_4^- 7850	3_4^- 8250
5^+ 6838		5_3^+ 6373	5_6^+ 6814		

TABLE I. (*Continued*).

Experiment[a] positive parity $2J_n^+$ Ex (keV)	Experiment[a] negative parity $2J_n^-$ Ex (keV)	$(sd)^3$ positive parity $2J_n^+$ Ex (keV)	ZBM positive parity $2J_n^+$ Ex (keV)	*psd* negative parity $2J_n^-$ Ex (keV)	ZBM negative parity $2J_n^-$ Ex (keV)
	3_5^- 6891			(3_4^- 7850)	(3_4^- 8250)
	7_4^- 6926			7_4^- 7347	7_4^- 7191
	1_3^- 6989			(1_2^- 6212)	(1_2^- 7156)
7^+ 7114		(7_3^+ 6297)	(7_6^+ 7883)		
	11_1^- 7166			11_1^- 6778	11_1^- 7818
$3^\pm$	1_4^- 7262			(1_3^- 8735)	(1_3^- 8253)
1^+ 7364		(1_3^+ 7820)	(1_4^+ 7621)		
5^+ 7540	$T=\frac{3}{2}$	5_1^+ 7816	$T=\frac{3}{2}$		
	? 7587			(5_4^- 6688)	(5_4^- 6840)
				(5_5^- 7514)	(5_5^- 7725)
3^+ 7661	$T=\frac{3}{2}$	3_1^+ 8110	$T=\frac{3}{2}$		
	1_5^- 7702			(1_4^- 8735)	(1_4^- 8253)
	? 7753			(7_5^- 8042)	(7_5^- 7461)
	Levels below 8 MeV—unmatched theory				
			5_7^+ 6879		
			9_3^+ 6939		
			9_4^+ 7819		
				9_3^- 8039	9_3^- 7418

[a]Reference 17.
[b]Multiplet in the (e,e') analysis.
[c]Spins in parentheses denote cases where the data in the figures are compared with theory even though the theoretical assignment has been made to another experimental level or is uncertain.
[d]Form factor is not obtained because of the large width of this state.
[e]Ex relative to experimental excitation energy of the lowest $\frac{1}{2}^-$ state. The calculated excitation energy of the lowest $\frac{1}{2}^-$ state is 2265 keV.

space omits the $p_{3/2}$ and $d_{3/2}$ orbits, and should therefore underpredict observed densities at least to the degree that these configurations are important in the range of excitation considered.

As mentioned in the previous section, we do not attempt to compare experimental form factors with ZBM predictions. These model results are thus invoked in Table I simply to rationalize the excess of experimentally observed positive-parity levels over those predicted in the SD calculation. To the extent that the ^{19}F ground state is 3p-0h, the 5p-2h and 7p-4h configurations of the ZBM space and the intruder states to which they give rise will not be directly excited in electron scattering. However, since these configurations can in principle mix with the 3p-0h configurations, the excitation strength from the SD space can be fragmented over the complete spectrum of positive-parity states. One issue which the present data addresses is the degree to which this mixing occurs in nature. This mixing could also generate excess strength over what is available within the SD space in addition to causing fragmentation, but the limitations of the ZBM model do not allow an adequate theoretical test of this aspect.

A. General features

In considering the electron scattering results, we first concentrate not on any individual level or group of levels but on the distribution of excitation strength over the entire low energy (Ex less than 8 MeV) part of the ^{19}F spectrum. We analyze this region by decomposing the spectra according to a variety of criteria. We separate the negative-parity level spectra from the positive-parity level spectra, the distributions of the strengths of the transverse excitation processes from those of the longitudinal processes, and, finally, the transition strengths at high values of momentum transfer from those at low momentum transfer. In each case, we compare the experimentally observed distributions with theoretical predictions. The multipolarities of the transitions do not emerge explicitly in these projections, but these multipolarities are implicit-

TABLE II. Electromagnetic transition rates from the $\frac{1}{2}^+$ ground state to final states J_f, Ex_f in ^{19}F.

	Experiment[a]			Theory		
L	$2J_f$	Ex_f (keV)	$B(L)$[b]	$2J_f$	Ex_f (keV)	$B(L)$[b]
			$T_f=\frac{1}{2}$			
$M1$	1^+	0	2.629[c]	1^+	0	2.911[b]
	$1^{(+)}$	5337	0.34(5)			
	1^+	5938	?	1^+	6084	0.0039
	1^+	6255	?			
	1^+	7364	?	1^+	7820	0.0207
$M1$	3^+	1554	0.15(9)	3^+	1698	0.0172
	3^+	3908	0.43(25)			
	3^+	5501	0.025			
	3^+	6497	?			
	3^+	6528	?	3^+	6627	0.128
				3^+	7728	0.290
$E2$	3^+	1554	?	3^+	1698	36.9
	3^+	3908	?			
	3^+	5501	?			
	3^+	6497	?			
	3^+	6528	?	3^+	6627	4.68
				3^+	7728	0.95
$E2$	5^+	197	62.8(7)	5^+	99	55.6
	5^+	4550	?	5^+	5155	4.16
	5^+	5107	?			
	5^+	5535	?			
	5^+	6282	17(6)	5^+	6373	1.35
				5^+	7285	2.33
$E1$	1^-	110	0.000 55(6)	1^-	110	0.0034
	$1^{(-)}$	5337	0.003 8(5)			
	1^-	6462	?	1^-	6212	0.0057
	1^-	6989	?	1^-	8735	0.0037
				1^-	8799	0.0040
$E1$	3^-	1459	0.000 9(2)	3^-	1900	0.007 1
	3^-	4556	0.000 28(23)	3^-	5071	0.000 32
	3^-	6088	0.004 7(13)	3^-	6346	0.000 92
	3^-	6787	0.005 0(13)	3^-	7850	0.001 5
				3^-	8542	0.000 19
				3^-	8647	0.000 12
$M2$	3^-	1459	?	3^-	1900	12.4
	3^-	4556	?	3^-	5071	0.015
	3^-	6088	?	3^-	6346	3.2
	3^-	6787	87(42)	3^-	7850	0.16
				3^-	8542	2.88
				3^-	8647	0.024

TABLE II. (*Continued*).

		Experiment[a]			Theory	
L	$2J_f$	Ex_f (keV)	$B(L)$[b]	$2J_f$	Ex_f (keV)	$B(L)$[b]
$M2$	5^-	1346	?	5^-	1507	1.46
	5^-	4682	?	5^-	4775	0.137
	5^-	5621	?	5^-	6030	0.049
				5^-	6688	0.083
				5^-	7514	1.93
	$T_f=\frac{3}{2}$					
$M1$	1^+	8791	?	1^+	9286	0.001 49
	3^+	7661	0.26(8)	3^+	8110	0.720
$E2$	3^+	7661	?	3^+	8110	0.57
	5^+	7540	?	5^+	7816	0.82

[a]Reference 17.
[b]$B(L)$ $J_i=\frac{1}{2}^+\rightarrow J_f$, $B(M1)$ in units of u_N^2, $B(E2)$ in units of e^2 fm^4, $B(M2)$ in units of u_N^2 fm^2, $B(E1)$ in units of e^2 fm^2.
[c]Magnetic moment in units of u_N.

ly a major factor in both the momentum transfer dependence and the relative strengths of transverse and longitudinal transitions.

These global views of the electroexcitation of ^{19}F and of the correspondence between experiment and theory for this system are presented in Figs. 1 and 2. Shown in the left center panel of Fig. 1 are the experimental data for scattering on the Teflon target at an angle of 90° and an energy of 271.5 MeV, and shown in the right center panel are data taken at 160° and 194.5 MeV. These two spectra, which are not plotted on the same cross section scale, emphasize, respectively, the longitudinal and transverse components of the scattering at a momentum transfer of 1.95 fm^{-1}.

The panels of bar graphs immediately above and below the experimental spectra represent the reductions of these data into (on the left) purely longitudinal and (on the right) purely transverse form-factor values for the momentum transfer of 1.95 fm^{-1}. The results for positive-parity states are plotted above the raw experimental spectra, those for negative-parity states below. In comparison with these plots of measured form-factor strength versus excitation energy, we show in the top (positive parity) and bottom (negative parity) panels the energy distribution of form-factor strength predicted from, respectively, the SD and PSD shell-model calculations for ^{19}F.

The measured distribution of positive-parity longitudinal strength at 1.95 fm^{-1} (panel LoEx$^+$) is dominated by the four lowest states in the spectrum, which have spins $\frac{1}{2}$, $\frac{5}{2}$, $\frac{3}{2}$, and $\frac{9}{2}$, respectively, and which are the only positive-parity states below 4 MeV excitation energy. Between 4 and 8 MeV, two dozen positive-parity states are known, but none is observed to have significant longitudinal strength. The predictions (panel LoTh$^+$) which correspond to these data give a good rendition of the positions and the relative and absolute values of these four dominant transitions.

In the 4—8 MeV region, the predicted number of levels is only about one-half of what is observed, while the aggregate amount of longitudinal strength predicted for this region is close to that which is observed. As we have mentioned, we interpret the excess of observed positive-parity levels in this region over what is predicted in the SD model calculations to the presence of multiparticle, multihole excitations of the ZBM-type. Their presence in the midst of the SD states appears to fragment the form factor strength over additional levels without significantly changing the total amount of this strength.

The lowest four positive-parity states also dominate the experimental (panel TrEx$^+$) and theoretical (panel TrTh$^+$) positive-parity spectra of the transverse excitation strength at 1.95 fm^{-1}. The relative strengths of these four levels are quite different in the transverse mode than in the longitudinal, but the measured values are again well reproduced by theory. The amount of transverse strength in the 4—8 MeV region is larger, relative to the low-lying strength in both the experimental and theoretical spectra, than was the case in the longitudinal spectra. The amount of experimental strength in this region appears to be somewhat greater than that predicted.

The distributions of longitudinal strength to negative-parity levels is displayed in the bottom two left-hand panels (LoEx$^-$ and LoTh$^-$) of Fig. 1. The spectra are dominated by one state, the first $\frac{5}{2}$ at 1.3 MeV, in the lower 4 MeV portion of the spectra and two states (the

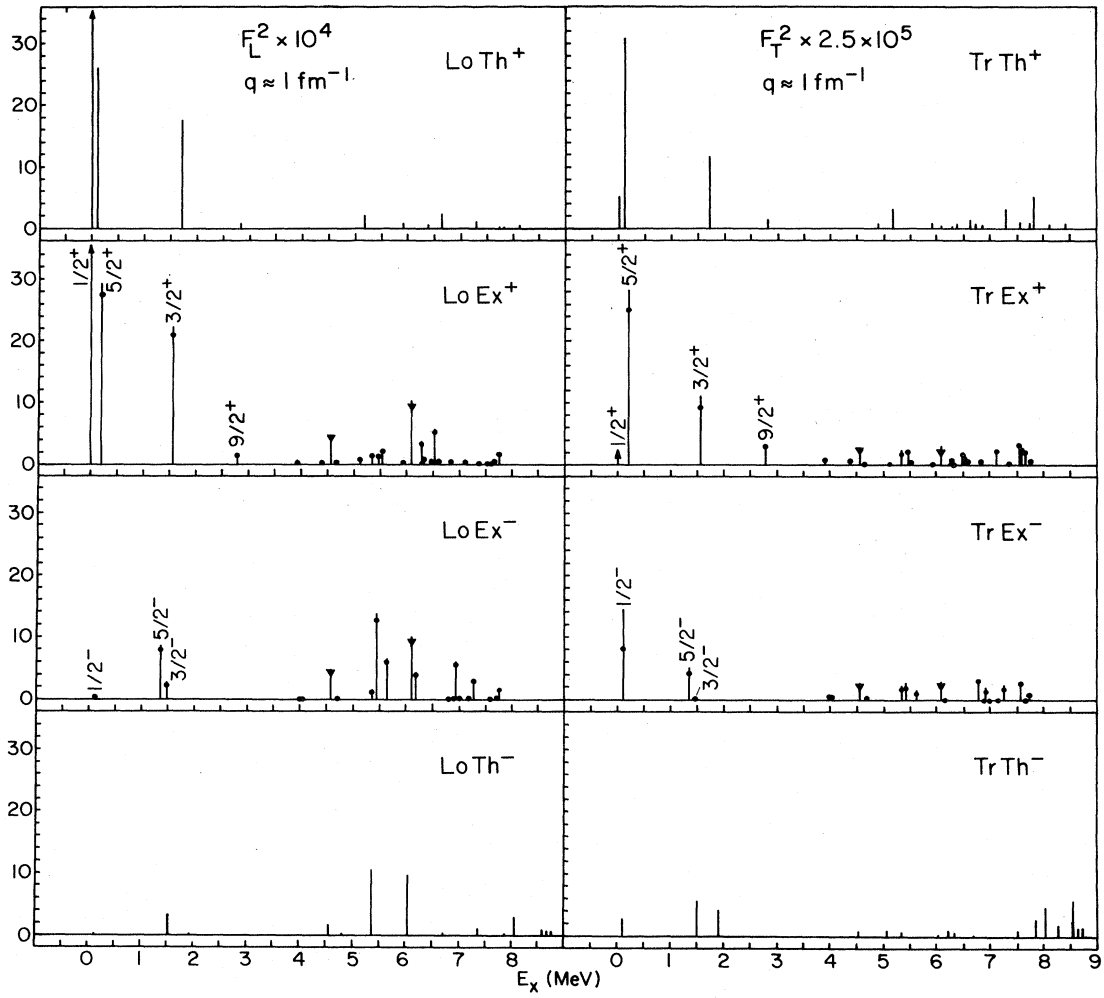

FIG. 2. Electroexcitation spectra of ^{19}F at $q = 1.0$ fm^{-1}. The raw spectra are not shown, but the LoTh$^+$, TrTh$^+$, LoEx$^+$, TrEx$^+$, LoEx$^-$, TrEx$^-$, LoTh$^-$, and TrTh$^-$ panels are obtained and displayed as described in the caption to Fig. 1.

second $\frac{7}{2}$ and third $\frac{5}{2}$) in the upper 4 MeV portion. The energy positions and relative and absolute strengths observed are reasonably well reproduced with the PSD predictions. Likewise, the number, position, and typical strengths of the dozen-odd weaker negative-parity levels which are observed are in overall accord with predictions.

The distributions of transverse strength to the negative-parity levels, shown in the lower two right-hand panels of Fig. 1, are quite different from the longitudinal distributions. The lowest $\frac{1}{2}$ state is the strongest observed in this distribution, and the higher lying $\frac{5}{2}$ and $\frac{7}{2}$ states are not prominent. The theoretical spectrum has a clear qualitative resemblance to the measured spectrum, but the differences in detail are more noticeable than in the other instances we have discussed.

In Fig. 2 we present distributions of experimental longitudinal and transverse form-factor values which are analogous to those shown in Fig. 1 but which correspond to a momentum transfer value of 1.0 fm^{-1}. We do not show in this figure the panels of raw data which we did in Fig. 1, but otherwise the presentation follows the same conventions. Overall, we expect Fig. 2 to emphasize lower multipolarity strength relative to that of Fig. 1. This is manifested in the different relative strengths observed (panels LoEx$^+$ and TrEx$^+$) for the lowest four positive-parity states in both the longitudinal and transverse distributions. Here, the $\frac{9}{2}$ state is much weaker and the $\frac{3}{2}$ much stronger than at 2 fm^{-1}. The longitudinal strength observed at higher excitations is greater than that predicted, but the predicted transverse strengths remain in good accord with observation. The observed distributions of strength for negative parity states, shown in the third panels from the top (LoEx$^-$ and TrEx$^-$) of Fig. 2, are not characterized by any striking patterns. The theoretical distributions shown in the bottom panels (LoTh$^-$ and TrTh$^-$) are in qualitative accord with these results.

In this first pass over our electron scattering data on ^{19}F, we have examined from a bird's eye view the qualitative aspects of its dependencies upon excitation energy, transition multipolarity, momentum transfer, parity, and

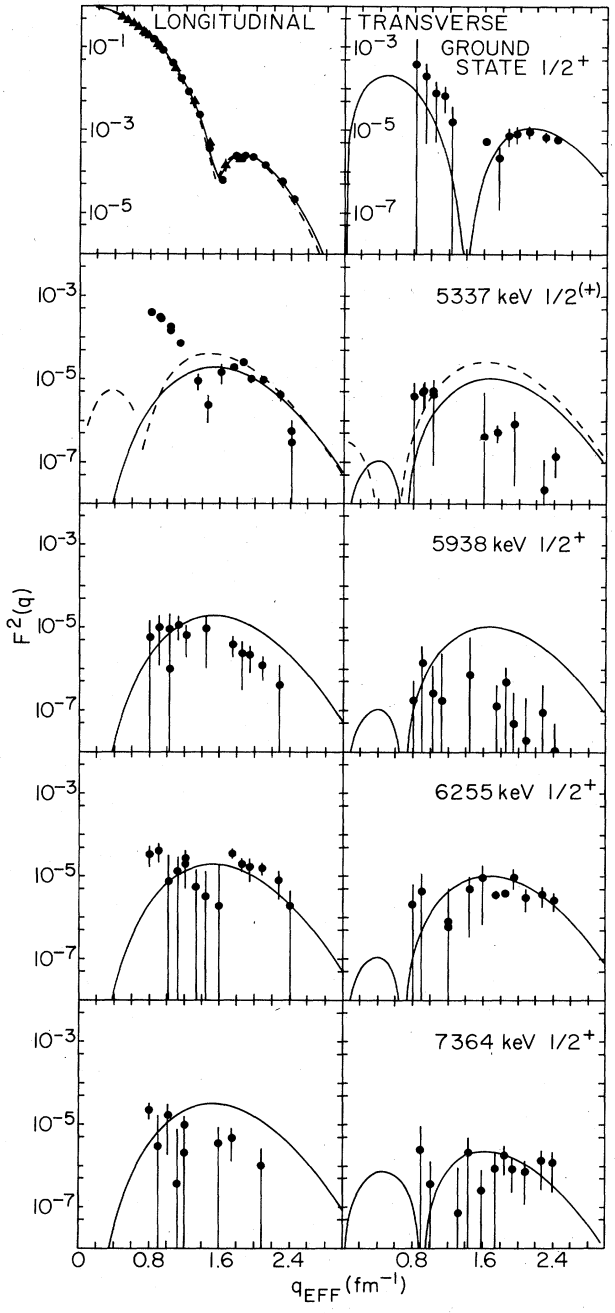

FIG. 3. Experimental and theoretical form factors for the $\frac{1}{2}^+$ levels observed in ^{19}F at 0.000, 5.337, 5.938, 6.255, and 7.364 MeV. Experimental values are indicated by the filled circles with error bars (present experiment) and filled triangles with error bars (data from Ref. 2). The solid curves are the predictions for the first (ground state), second (5.337, 5.938, and 6.255 MeV level), and third (7.364 MeV level) SD $\frac{1}{2}^+$ states of ^{19}F. The dashed curves in the panel for the 5.337 MeV level are the predictions for the first PSD $\frac{1}{2}^-$ state. All calculations were carried out using harmonic-oscillator radial wave functions with an oscillator length parameter $b=1.806$ fm. For the elastic longitudinal elastic scattering we also show (dashed line) the form factor calculated with $b=b_{\rm rms}=1.833$ fm (see Sec. V B).

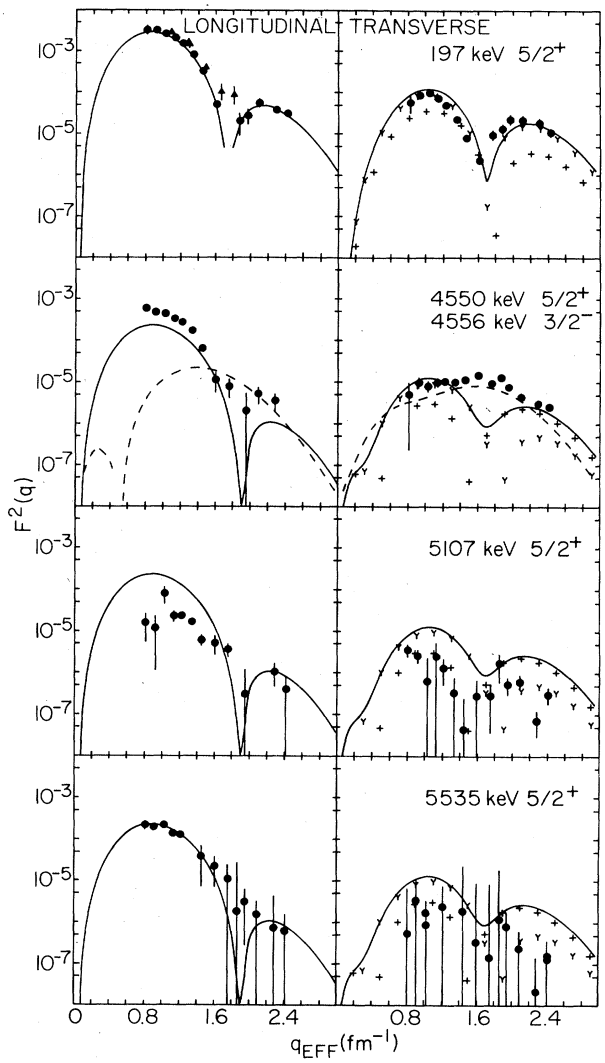

FIG. 4. Experimental and theoretical form factors for the $\frac{5}{2}^+$ levels observed in ^{19}F at 0.197, 4.550, 5.107, and 5.535 MeV. Experimental values are indicated by the filled circles with error bars (present experiment) and filled triangles with error bars (data from Ref. 2). The solid curves are the predictions for the first (0.197 MeV level) and second (4.555, 5.107, and 5.535 MeV levels) SD $\frac{5}{2}^+$ states of ^{19}F. The "+" and "Y" symbols in the transverse panels indicate, respectively, the separate $E2$ and $M3$ contributions to these form factors. The dashed lines in the 4.555 MeV panel are the predictions for the second PSD $\frac{3}{2}^-$ state, since the 4.556 MeV $\frac{3}{2}^-$ level of ^{19}F is unresolved from this $\frac{5}{2}^+$.

the transverse-longitudinal character of the scattering process. We have found that the shell-model predictions for the response of ^{19}F to the variety of different operators provided by the electron-scattering probe are in good overall agreement with the global aspects of the data. We now turn to detailed examinations of individual form factors and concentrate on determining the degree to which

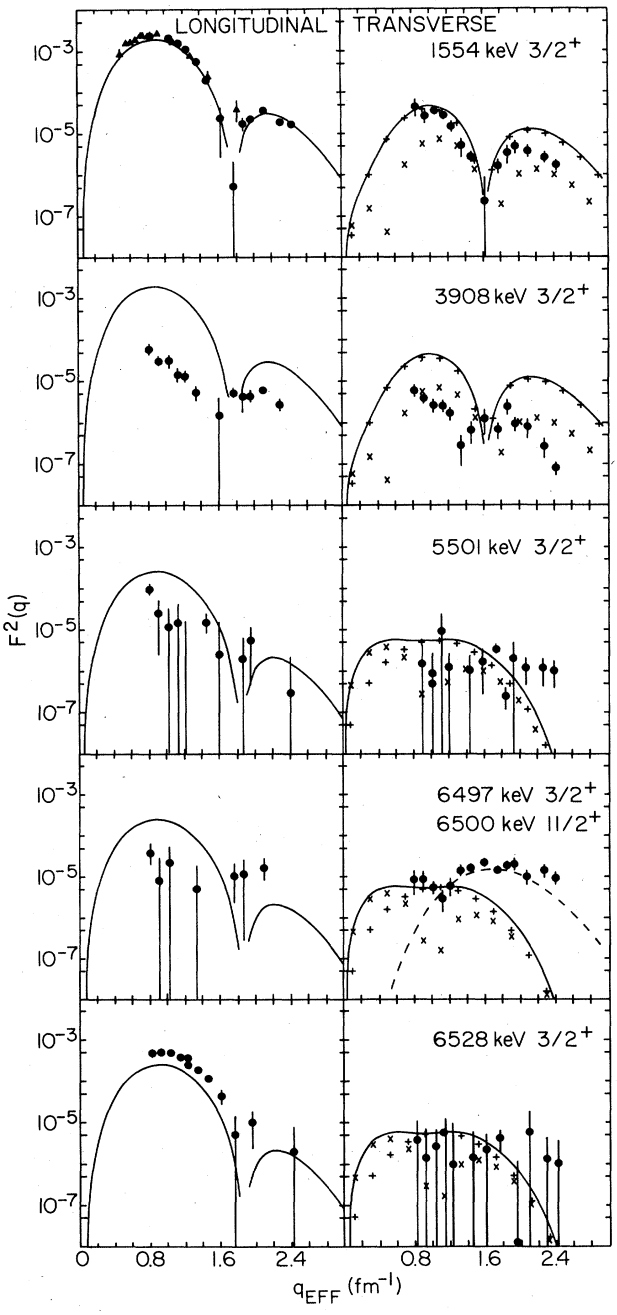

FIG. 5. Experimental and theoretical form factors for the $\frac{3}{2}^+$ levels observed in ^{19}F at 1.554, 3.908, 5.501, 6.497, and 6.528 MeV. Experimental values are indicated by the filled circles with error bars (present experiment) and filled triangles with error bars (data from Ref. 2). The solid curves are the predictions for the first (1.554 and 3.908 MeV levels) and second (5.501, 6.497, and 6.528 meV levels) SD $\frac{3}{2}^+$ states of ^{19}F. The "+" and "×" symbols in the transverse panels indicate, respectively, the separate $E2$ and $M1$ contributions to these form factors. The 6.497 MeV level is seen experimentally as a doublet with the 6.500 MeV $\frac{11}{2}^+$ level, whose calculated form factor is given by the dashed line.

quantitative detailed agreement between theory and experiment can be achieved on a state by state basis.

B. The positive-parity ground-state band: States with $\frac{1}{2}^+$, $\frac{3}{2}^+$, $\frac{5}{2}^+$, $\frac{9}{2}^+$, and $\frac{13}{2}^+$

A variety of experimental evidence suggests that the lowest observed states of spin parities $\frac{1}{2}^+$, $\frac{3}{2}^+$, $\frac{5}{2}^+$, and $\frac{9}{2}^+$ are members of a $K^\pi=\frac{1}{2}^+$ rotational band. Independently of any presuppositions about the nature of these states, the comparison of theoretical and experimental energies in Table I requires that the lowest such states in the model spectra correspond to these experimental states if the model is to be taken seriously. Thus, these model-nature correspondences are the most secure ones we have. The data for these states are the most complete and precise we have from this experiment. The form factors for these four states yield examples of longitudinal $C0$, $C2$, and $C4$ scattering and transverse $M1$, $E2$, $M3$, $E4$, and $M5$ scattering. The data extend over a wide enough range of momentum transfer that details of the radial wave functions are brought into the test. We wish to establish for these optimum cases how well the straightforward $(sd)^3$ shell-model approach can reproduce this full range of phenomena.

The longitudinal form factor for the ground-state (elastic) scattering, shown in Fig. 3, has already been examined in our discussion of the appropriate oscillator parameter for the radial wave functions. The transverse scattering from this state, also shown in Fig. 3, indicates that the effective radius of the magnetization distribution is consistent with the charge distribution (see also Ref. 54). Also, in the context of the SD shell-model wave function, the magnetic strength of this state at momentum transfers up to 2.5 fm^{-1} is consistent with the magnetic moment (see Table II).

The measured longitudinal and transverse form factors for the first observed $\frac{5}{2}^+$ level (at 0.197 MeV) in ^{19}F are shown in comparison with the predictions of the corresponding SD state in Fig. 4. We see that the longitudinal form factor, measured with good precision to 2.4 fm^{-1}, is well reproduced by the SD form factor combined with the effective-charge transition density as described in Sec. V. The former factor is completely consistent with the measured and calculated $B(E2)$ values of Table II. The experimental transverse form factor, also determined with good precision, has its maximum and minimum in the same positions as does the longitudinal. The SD form factor correctly predicts both this different profile and the overall magnitude of the transition. The $M3$ component of the transverse scattering dominates the $E2$ according to the calculation.

The measured longitudinal and transverse form factors of the first observed $\frac{3}{2}^+$ level (at 1.554 MeV) in ^{19}F are shown in comparison with the predictions of the corresponding SD state in Fig. 5. The theoretical values of the longitudinal form factor are too small by about a factor of 1.3 at the lower values of momentum transfer. The $B(E2)$ for this transition is unmeasured, so that a correspondence between the $q\rightarrow 0$ value and the scattering data is not possible. Qualitatively, the agreement between

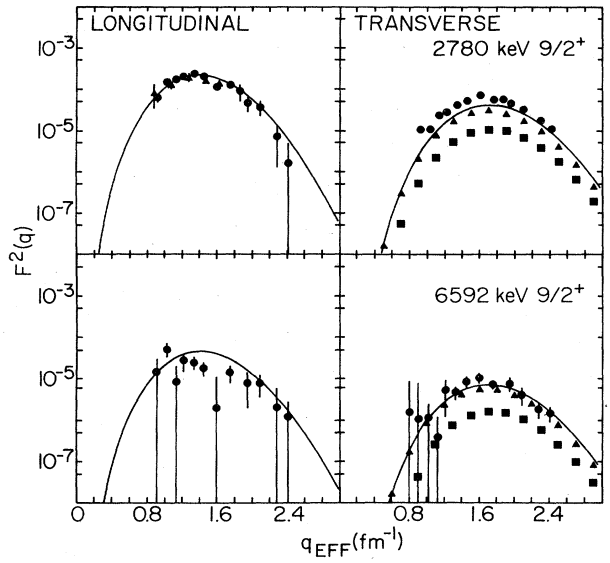

FIG. 6. Experimental and theoretical form factors for the $\frac{9}{2}^+$ levels observed in ^{19}F at 2.780 and 6.592 MeV. Experimental values are indicated by the filled circles with error bars (present experiment) and filled triangles with error bars (data from Ref. 2). The solid curves are the predictions for the first (2.789 MeV level) and second (6.592 MeV level) SD $\frac{9}{2}^+$ states of ^{19}F. The "square" and "triangle" symbols in the transverse panels indicate, respectively, the separate $E4$ and $M5$ contributions to these form factors.

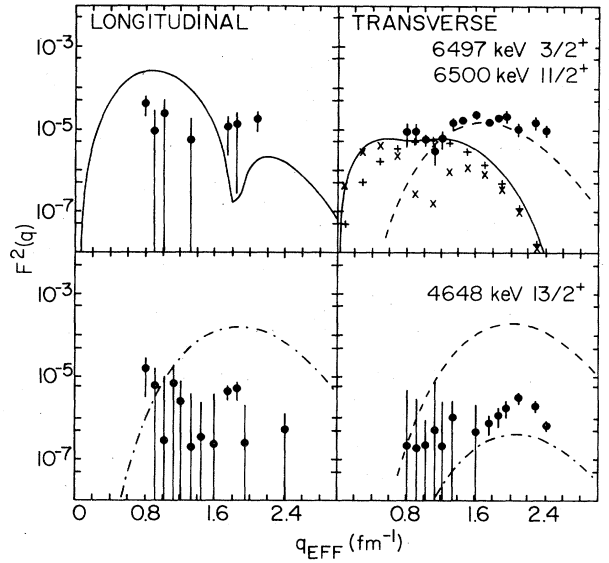

FIG. 7. Experimental and theoretical form factors for the $\frac{11}{2}^+$ and $\frac{13}{2}^+$ levels observed in ^{19}F at 6.500 and 4.648 MeV, respectively. Experimental values are indicated by the filled circles. The curves in the panel for the 4.648 MeV level are the predictions for the $f_{7/2}$ models discussed in the text. The curves in the panel for the 6.500 MeV level are the predictions for the second $\frac{3}{2}^+$ (solid curve) and first $\frac{11}{2}^+$ (dashed curve) SD states. The "+" and "×" symbols in the transverse panels indicate, respectively, the separate $E2$ and $M1$ contributions to the $\frac{3}{2}^+$ form factor.

theory and experiment does not suggest major problems with the model formulation.

The experimental and theoretical transverse form factors for this state, although not so large, are reminiscent of those of the $\frac{5}{2}^+$ state in terms of overall shape. However, theory is significantly too large relative to experiment in the region of the second maximum, and it must be remembered that the contributing terms to this transition are $M1$ and $E2$, rather than $E2$ and $M3$. Here the dominant contributions to the form factor are predicted to come from the electric rather than the magnetic term. However, the measured value of $B(M1)$ is much larger than is predicted, as can be seen from Table II. A cancellation of the $M1$ term at small q is indicated from Fig. 5. It is difficult to draw from these various facts any definitive conclusions.

The measured longitudinal and transverse form factors of the first $\frac{9}{2}^+$ level (at 2.780 MeV) of ^{19}F are shown in comparison with the SD predictions in Fig. 6. The multipolarities which are involved in this transition are $C4$, $E4$, and $M5$. Both the shape and the magnitude scale of the longitudinal ($C4$) data are accurately reproduced by theory throughout the range of measurement. This $E4$ relationship between the ground state and this level supplements what is known about the relationships of the $\frac{1}{2}^+$, $\frac{3}{2}^+$, $\frac{5}{2}^+$, and $\frac{9}{2}^+$ states from their $E2$ connections. All of these experimentally determined relationships are reasonably consistent with the corresponding shell-model predictions. The theoretical transverse form factor is dominated by the $M5$ component. It agrees in shape with experiment, the maximum of these form factors falling approximately at 1.6 fm^{-1} rather than the 1.2 fm^{-1} characteristic of the longitudinal shapes. The theoretical envelope falls below experiment by a factor of about 1.4, but we cannot say whether this deficiency is to be associated with the $E4$ or the $M5$ component.

The first $\frac{13}{2}^+$ level (at 4.648 MeV) in ^{19}F is connected to the first $\frac{9}{2}^+$ level by a strong $E2(C2)$ transition. Hence it can be thought of as an extension of the ground state band. The measured limits on its longitudinal and transverse form factors are shown in Fig. 7. This state can be reached from the $\frac{1}{2}^+$ ground state only by a $C6$, $E6$, or $M7$ transition. The largest multipolarity which is consistent with a one-body process in the *sd*-shell space is $M5$. Thus, observed $C6$ strength for this transition can be interpreted as a measure of the role of higher-spin orbits (presumably $f_{7/2}$) in these states. We compare the longitudinal data to the form factor calculated for the 0^+ to 6^+ $C6$ transition associated with a two-neutron $(f_{7/2})^2$ state under the assumption of an effective charge of $0.35e$ for the neutrons. In the region of the theoretical maximum, the measured strength is 2% of this simple $(f_{7/2})^2$ limit. This suggests an $f_{7/2}$ pairing amplitude in the ground state of ^{19}F of no more than about 0.15.

The transverse form factor for this state presumably

would be generated by a 0^+-7^+ $M7$ transition in the neutron-proton $(f_{7/2})^2$ space. (The transverse $E6$ form factor in this model vanishes.) The data are only 1% of the strength of this calculation. Again, this simple comparison suggests that the limit on $f_{7/2}$ admixtures in the ^{19}F ground state is of order of 0.10 in amplitude. This degree of $f_{7/2}$ (or higher) orbit admixtures is not inconsistent with experiment or qualitative intuition. At this level of transition strength it is quite possible that there could be significant contributions from multiple-step processes. At the present time no theoretical calculations are available for these multiple-step processes.

C. Relationship of $\frac{11}{2}^+$ and $\frac{7}{2}^+$ states to the ground-state band and to shell-model counterparts in general

Unique identities of the $\frac{7}{2}^+$ and $\frac{11}{2}^+$ members of the "ground state band" of ^{19}F are not easy to establish. The only $\frac{11}{2}^+$ level in the range of excitation energy covered in our data is that identified at 6.500 MeV. A $\frac{3}{2}^+$ level at 6.497 MeV cannot be resolved from it. In Fig. 7 we plot the longitudinal and transverse data for the peak observed at 6.50 MeV together with the predictions for the second SD $\frac{3}{2}^+$ state and the first SD $\frac{11}{2}^+$ state. There is no contribution from the $\frac{11}{2}^+$ state to the longitudinal form factor, and the $\frac{3}{2}^+$ prediction is much larger than the data. However, the $M5$ transverse form factor for the $\frac{11}{2}^+$ state yields excellent agreement with the higher-q transverse data, with the $M1$ and $E2$ contributions for the $\frac{3}{2}^+$ state being consistent with the sparse low-q points. We conclude from these comparisons that the $\frac{11}{2}^+$ level is significantly excited at large q in the transverse mode, and that the SD predictions are in good accord with observation. These results are similar to those obtained for the first $\frac{9}{2}^+$ level, with the difference being that for $\frac{11}{2}^+$ there is no $C4$ or $E4$ contribution possible.

The relationships between the several $\frac{7}{2}^+$ states observed below 8 MeV and the various model predictions are at best murky. Experimental and theoretical results for these states are shown in Figs. 8 and 9. There is no clear candidate for the ground-state-band member. The first observed $\frac{7}{2}^+$ level of ^{19}F, at 4.378 MeV, has a relatively weak longitudinal ($C4$) form factor, while the second, at 5.464 MeV, is five times stronger. The predictions for the first two SD $\frac{7}{2}^+$ states are consistent with these data. The fit to the second, stronger state is good, while the calculated magnitudes for the first, weaker state are larger than the almost vanishing measured values.

In the case of the transverse form factors for these states, no matter what combination of theory and experiment is chosen, the predicted shapes are in rather poor agreement with the data. The third experimental $\frac{7}{2}^+$ level is identified in the midst of an unresolvable triplet at 6.08 MeV. No useful conclusions can be drawn from comparisons of the observed longitudinal form factor for this peak, but the higher-q transverse data are well fitted by the predictions for the second SD $\frac{7}{2}^+$ states. This renders the association of this model state with the level

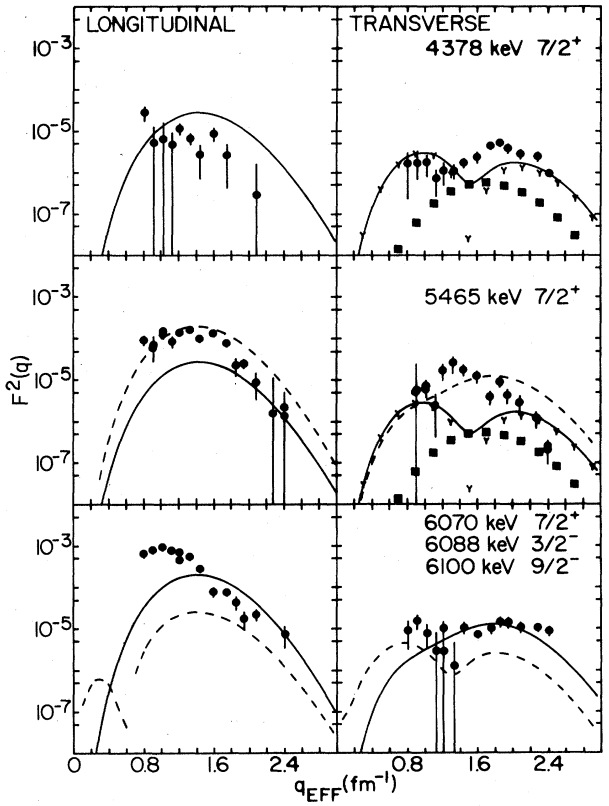

FIG. 8. Experimental and theoretical form factors for the $\frac{7}{2}^+$ levels observed in ^{19}F at 4.378, 5.465, and 6.070 MeV. Experimental values are indicated by the filled circles. The solid curves are the predictions for the first (4.378 and 5.465 MeV levels) and second (6.070 MeV level) SD $\frac{7}{2}^+$ states of ^{19}F. The dashed lines in the panel for the 5.465 MeV level are the predictions for the second SD $\frac{7}{2}^+$ state, and, in the panel for the 6.070 MeV level, for the second PSD $\frac{3}{2}^-$ state. The "Y" and "square" symbols in the transverse panels indicate, respectively, the separate $M3$ and $E4$ contributions to the first SD $\frac{7}{2}^+$ state.

observed at 5.464 MeV suspect. We note that the ZBM calculation yields three $\frac{7}{2}^+$ states in this region, in accord with experiment, rather than the two which are predicted in the SD spectrum. The ambiguity in matching the SD form factors with the data presumably is a consequence of the mixing of an extra, core-excited $\frac{7}{2}^+$ state into its SD neighbors.

Additional $\frac{7}{2}^+$ levels are identified at excitation energies of 6.330, 7.114, and, perhaps, 6.554 MeV. Their form factors are shown in Fig. 9, together with the predictions for the second and third SD states. The predictions for the second SD state are in reasonable agreement with the data for the 6.330 MeV level, leaving the "true" experimental correspondent for this state even more uncertain. The third SD $\frac{7}{2}^+$ state is predicted to have very weak longitudinal and transverse form factors. This is consistent with the data for the 6.554 MeV level, but it is in disagreement with, in particular, the transverse data for

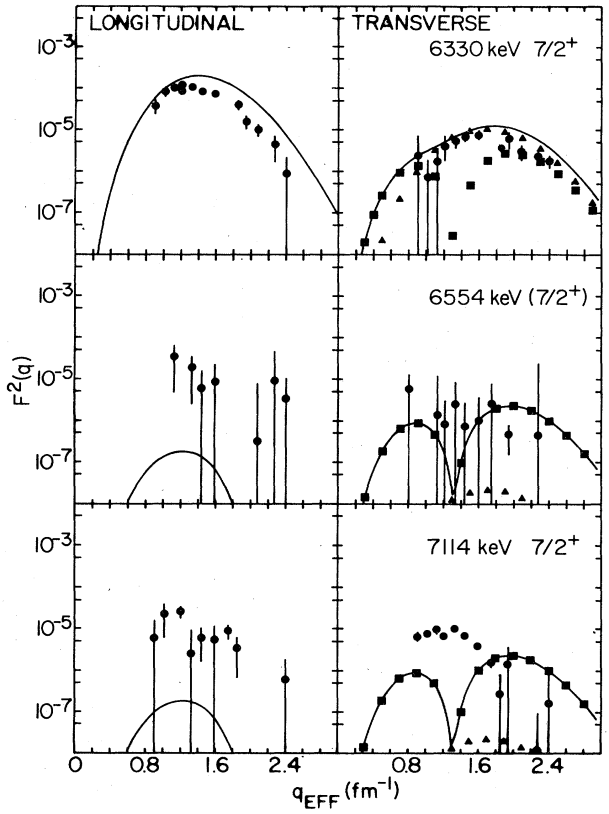

FIG. 9. Experimental and theoretical form factors for the $\frac{7}{2}^+$ levels observed in ^{19}F at 6.330, 6.554, and 7.114 MeV. Experimental values are indicated by the filled circles. The solid curves are the predictions for the second (6.330 MeV level) and third (6.554 and 7.114 MeV levels) SD $\frac{7}{2}^+$ states of ^{19}F. The "square" and "triangle" symbols in the transverse panels indicate, respectively, the separate $M3$ and $E4$ contributions to these form factors.

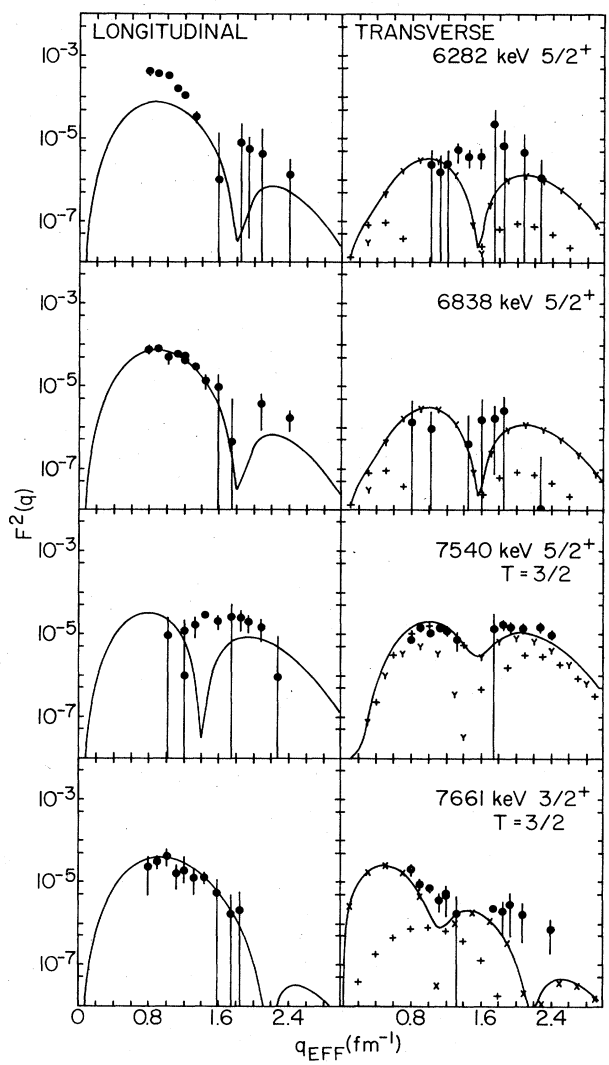

FIG. 10. Experimental and theoretical form factors for the $\frac{5}{2}^+$ levels observed in ^{19}F at 6.282, 6.838, and 7.540 MeV and the $\frac{3}{2}^+$ level observed at 7.661 MeV. Experimental values are indicated by the filled circles. The solid curves are the predictions for the third (6.282 and 6.838 MeV levels) $T=\frac{1}{2}$ SD $\frac{5}{2}^+$ state, the first (7.540 MeV level) $T=\frac{3}{2}$ SD $\frac{5}{2}^+$ state and the first (7.661 MeV level) $T=\frac{3}{2}$ SD $\frac{3}{2}^+$ state. The "+," "×," and "Y" symbols in the transverse panels indicate, respectively, the individual $E2$, $M1$, and $M3$ contributions to these form factors.

the 7.114 MeV level. The ZBM spectrum continues to be more dense in $\frac{7}{2}^+$ states at these energies than is the SD spectrum, but even the ZBM calculation seems to underpredict the observed density. The evidence suggests that the SD and ZBM states are so intermixed that it is not meaningful to make a one-to-one comparison between experiment and theory.

D. Other positive-parity states

Beyond the levels we have discussed so far, one other $\frac{9}{2}^+$ and three, possibly four, $\frac{1}{2}^+$ levels are identified in the experimental spectrum of ^{19}F below 8 MeV. Four and a possible fifth additional $\frac{3}{2}^+$ states with $T=\frac{1}{2}$ are found in this region, together with the $T=\frac{3}{2}$, $\frac{3}{2}^+$ level at 7.661 MeV. Five more $T=\frac{1}{2}$, $\frac{5}{2}^+$ states are known, together with the $T=\frac{3}{2}$, $\frac{5}{2}^+$ state at 7.540 MeV. The form factors measured for these states are compared with several of the SD predictions in Figs. 3–6, 10, and 11. We discuss the comparisons of these predictions with the data to further clarify the extent to which meaningful correspondences can be drawn between the higher-lying SD model states and experimental levels at comparable energies.

The only $\frac{9}{2}^+$ level in ^{19}F known below 8 MeV, other than the 2.780 MeV member of the ground band, is found at 6.592 MeV. Its measured longitudinal and transverse form factors are smaller than those of the lower $\frac{9}{2}^+$ but similar in shape. The predictions for the second SD $\frac{9}{2}^+$

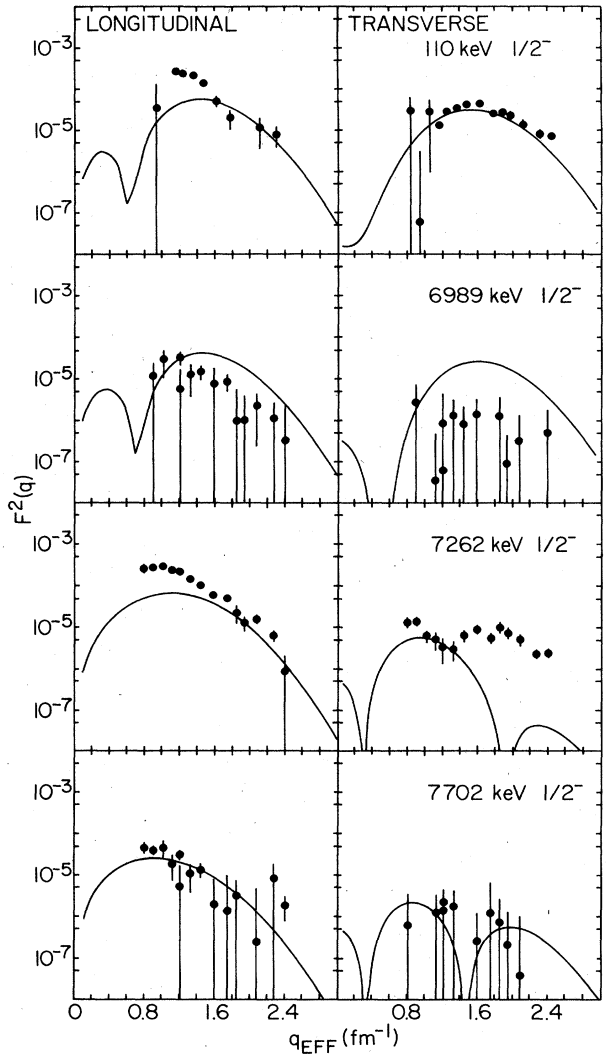

FIG. 11. Experimental and theoretical form factors for the $\frac{1}{2}^-$ levels observed in ^{19}F at 0.110, 6.989, 7.262, and 7.702 MeV. Experimental values are indicated by the filled circles. The solid curves are the predictions for the first (0.110 MeV level), second (6.989 MeV level), third (7.262 MeV level), and fourth (7.702 MeV level) $\frac{1}{2}^-$ PSD states of ^{19}F.

fit these data well, as can be seen in Fig. 6.

Data and predictions for the higher-lying $\frac{1}{2}^+$ levels are shown in Fig. 3. The $\frac{1}{2}^+$ level at 5.337 MeV has only a tentative positive-parity assignment. Its longitudinal form factor is radically different at low q values from the $C0$ shape of the form factor of the second SD $\frac{1}{2}^+$ state, and there is equally poor agreement between the experimental transverse form factors and those calculated from the SD model. The $C1$ form factor calculated from the first PSD $\frac{1}{2}^-$ state also fails altogether to fit the measured shape. The identity and nature of the 5.337 MeV state is thus uncertain in the present context. The ZBM spectrum has a $\frac{1}{2}^+$ state at 5 MeV, but overall is missing one $\frac{1}{2}^+$ state relative to experiment, if the 5.334 MeV is counted. The predictions for the second SD $\frac{1}{2}^+$ state are in relatively good agreement with the data for both the 5.938 and 6.255 MeV $\frac{1}{2}^+$ levels, with the 6.255 MeV level being preferred as the SD counterpart on the basis of a somewhat better fit of the form factors and, independently, on the basis of a significant stripping spectroscopic factor.[17] The form factors for the third SD $\frac{1}{2}^+$ state are in agreement within experimental errors with the data for the 7.364 MeV level.

Data and predictions for the second, third, and fourth experimentally identified $\frac{5}{2}^+$ levels, at 4.550, 5.107, and 5.535 MeV, are shown in Fig. 4. There is only one SD $\frac{5}{2}^+$ state in this range, although there are three ZBM states. As can be seen in Fig. 4, the single SD longitudinal form factor is too small for the second experimental level, too large for the third, and a good fit for the fourth. A $\frac{3}{2}^+$ level at 4.556 MeV is unresolved from the second $\frac{5}{2}^+$. The calculated form factors for the second PSD $\frac{3}{2}^-$ state do not improve the longitudinal comparison but seem to provide a fit to the transverse data. Altogether, these results suggest a tentative association of the 5.535 MeV level with the second SD $\frac{5}{2}^+$ state.

Date and predictions for the fifth and sixth $T=\frac{1}{2}$, $\frac{5}{2}^+$ levels, at 6.282 and 6.838 MeV, and the $T=\frac{3}{2}$, $\frac{5}{2}^+$, and $\frac{3}{2}^+$ levels, at 7.540 and 7.661 MeV, are shown in Fig. 10. The longitudinal form factor for the 6.282 MeV level is much larger than the prediction for the third SD $\frac{5}{2}^+$ state at low values of momentum transfer. Also, the transverse form factor is in poor agreement. The same predictions are in rather good agreement with the data for the 6.838 MeV level and it appears reasonable to associate this level with this model state. The experimental and theoretical longitudinal form factors for the $T=\frac{3}{2}$, $\frac{5}{2}^+$ state are each small, but they do not have the same shape. However, the combination of $E2$ and $M3$ transverse form factors predicted for this state are in good agreement with the corresponding data. In the case of the $T=\frac{3}{2}$, $\frac{3}{2}^+$ level, both the longitudinal and transverse predictions are in reasonable agreement with the data.

The second, third, fourth, and fifth $\frac{3}{2}^+$ level are identified at energies of 3.908, 5.501, 6.497, and 6.528 MeV, respectively. The unresolved 6.497 MeV level has already been discussed in conjunction with the $\frac{11}{2}^+$ level. The others are shown in comparison with predictions for the second SD $\frac{3}{2}^+$ state in Fig. 5. The longitudinal form factors of the 3.908, 5.501, and 6.497 MeV levels are much smaller than the prediction, while the data for the 6.528 MeV level are about a factor of 2 greater than theory. Little can be inferred from the transverse form factors of these states. It appears from these comparisons that the 6.528 MeV level is too strong to be properly associated with the second SD $\frac{3}{2}^+$ state.

E. Negative-parity levels

Levels with $\frac{1}{2}^-$ assignments are identified in ^{19}F at 0.110, 6.429, 6.989, 7.262, and 7.702 MeV. Data and calculations are shown in Fig. 11. The most significant form

factor associated with these levels is the transverse component of the 0.110 MeV level. The predicted transverse form factor for the first PSD state gives a good fit to these data. The low-q longitudinal data for this level greatly exceed the corresponding prediction, even though the experimental $B(E1)$ ($q=0$) value is smaller than theory (see Table II). The 6.429 MeV level cannot be detected in our spectra. The higher $\frac{1}{2}^-$ levels have form factors which disagree in various ways with the predictions, as shown. In comparison to the $C1$ theory, the longitudinal data seem to be systematically too large at the smaller q values relative to larger values of q.

Levels with $\frac{3}{2}^-$ assignments are identified in ^{19}F at 1.459, 4.556, 6.088, 6.787, and 6.891 MeV. Data and predictions are shown in Fig. 12. The longitudinal form factor for the 1.459 MeV level is completely different from the prediction for the first PSD $\frac{3}{2}^-$ state. The 4.556 MeV level is unresolved from the neighboring $\frac{5}{2}^+$ level. The data exceed the combined predictions at low q for the longitudinal component, but together seem to successfully account for the transverse component. The 6.088 MeV level is unresolved from neighboring $\frac{7}{2}^+$ and $\frac{9}{2}^-$ levels. Again, the longitudinal data exceed predictions at low q, while at higher q and in the transverse mode, the $\frac{7}{2}^+$ contributions seem to dominate. The longitudinal and transverse data for the 6.787 MeV level seem to be well accounted for by the predictions for the fourth PSD $\frac{3}{2}^-$ state. The transverse data for the 6.891 MeV level is also in fairly good agreement with the predictions for the fourth PSD state but the longitudinal data is very weak compared to the theory, suggesting that this level should not be associated with the fourth PSD state. The fifth PSD state (not shown in Fig. 12) lies 0.689 MeV above the fourth. The calculated longitudinal form factor for the fifth state is small (peaks at a value of 2×10^{-6}) compared to the fourth state, while the transverse form factors for the fourth and fifth states are similar in shape and magnitude.

Levels with $\frac{5}{2}^-$ spin assignments are identified in ^{19}F at 1.346, 4.682, and 5.621. A possible $\frac{5}{2}^-$ state occurs at 7.587 MeV. Data and predictions are shown in Fig. 13. The first $\frac{5}{2}^-$, at 1.346 MeV, has large longitudinal and transverse form factors. The predictions for the first PSD $\frac{5}{2}^-$ are in qualitative accord with these data, falling too low at low q in the longitudinal case and too high overall in the transverse case. The experimental and theoretical form factors for the second $\frac{5}{2}^-$ state are all very small. The longitudinal form factor for the third level, at 5.623 MeV, is very strong, but the transverse component is very weak. The predictions for the third PSD state are in good agreement with these results, failing only in rising above the longitudinal data at low q. The predictions for the fourth PSD $\frac{5}{2}^-$ state are not in drastic disagreement with the data for the 7.587 MeV level.

Levels with $\frac{7}{2}^-$ spin-parity assignments are identified in ^{19}F at 3.999, 5.418, 6.161, and 6.926 MeV. A possible $\frac{7}{2}^-$ level occurs at 7.753 MeV. Data and calculations are shown in Fig. 14. The lowest 3.999 MeV level has rather weak form factors, in agreement with the predictions for the first PSD $\frac{7}{2}^-$ state. The experimental shape for the

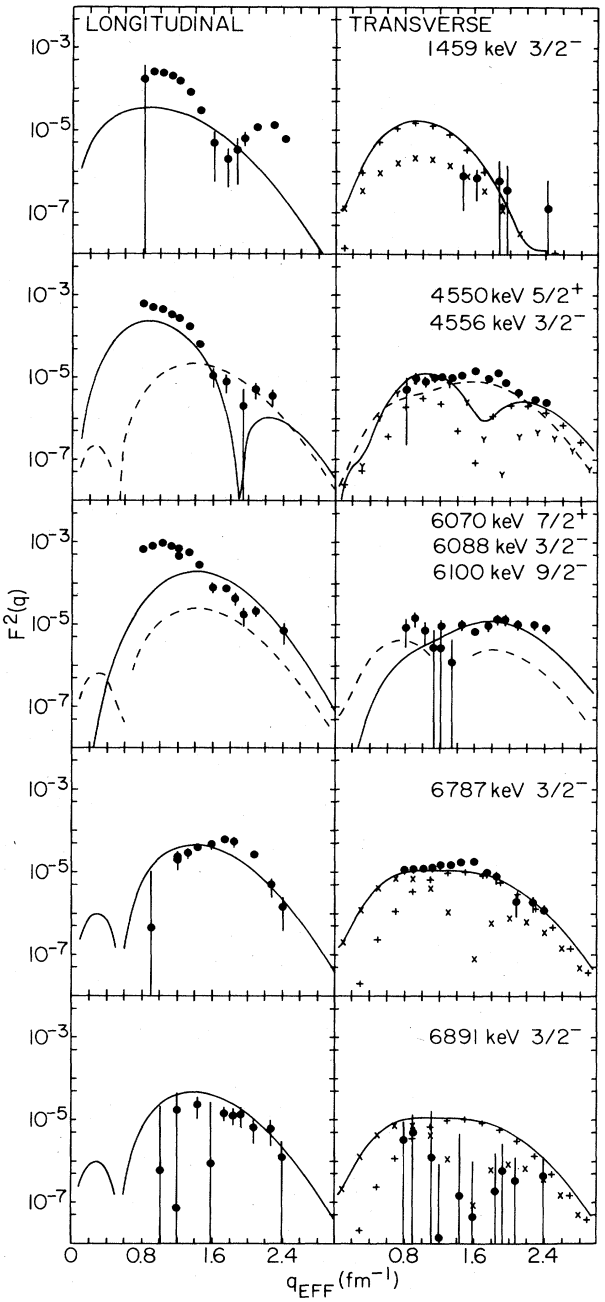

FIG. 12. Experimental and theoretical form factors for the $\frac{3}{2}^-$ levels observed in ^{19}F at 1.459, 4.556, 6.088, 6.787, and 6.891 MeV. Experimental values are indicated by the filled circles. The prediction for the first PSD $\frac{3}{2}^-$ state is shown by the solid curve in the 1.459 MeV panel. The predictions for the second and third PSD $\frac{3}{2}^+$ states are shown by the dashed lines in the 4.556 and 6.088 MeV panels, respectively, where the solid lines show the positive-parity alternatives. The prediction for the fourth PSD $\frac{3}{2}^-$ state is shown in the 6.787 and 6.891 MeV panels. The "$\times$" and "$+$" symbols in the transverse panels for the 1.459, 6.787, and 6.891 MeV levels indicate, respectively, the separate $E1$ and $M2$ contributions to these form factors. (For the 4.556 MeV level the decomposition shown is for the SD $\frac{5}{2}^+$, as described in the caption to Fig. 4.)

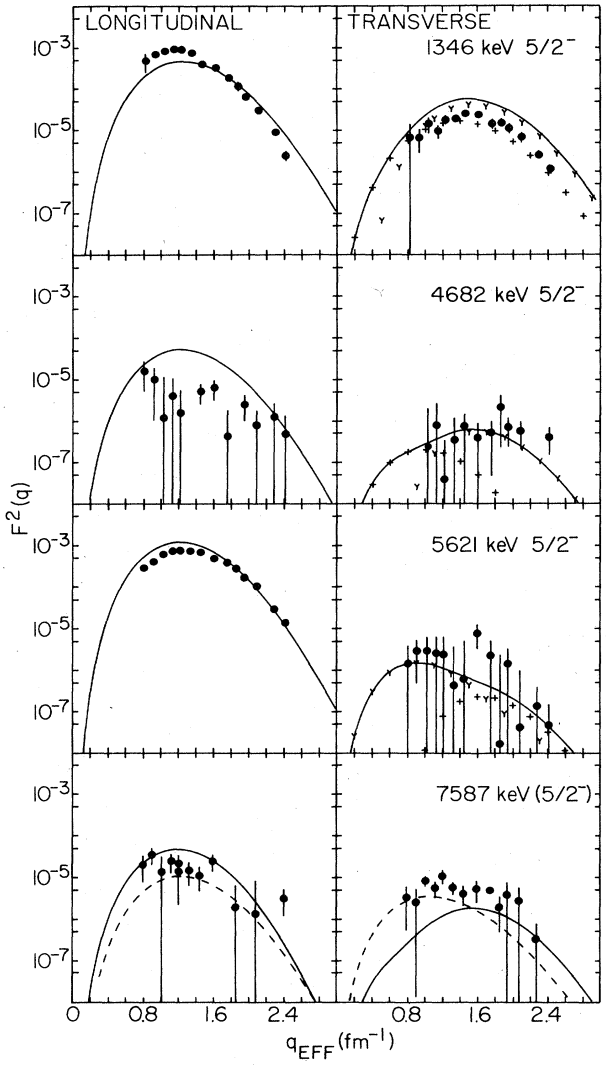

FIG. 13. Experimental and theoretical form factors for the $\frac{5}{2}^-$ levels observed in ^{19}F at 1.346, 4.682, 5.621, and 7.587 MeV. Experimental values are indicated by the filled circles. The solid curves are the predictions for the first (1.346 MeV level), second (4.682 MeV level), third (5.621 MeV level), and fourth (7.587 MeV level) PSD $\frac{5}{2}^-$ states of ^{19}F. The prediction for the third state is also shown by the dashed curve in the last panel. The "+" and "Y" symbols in the transverse panels indicate, respectively, the separate $M2$ and $E3$ contributions to these form factors.

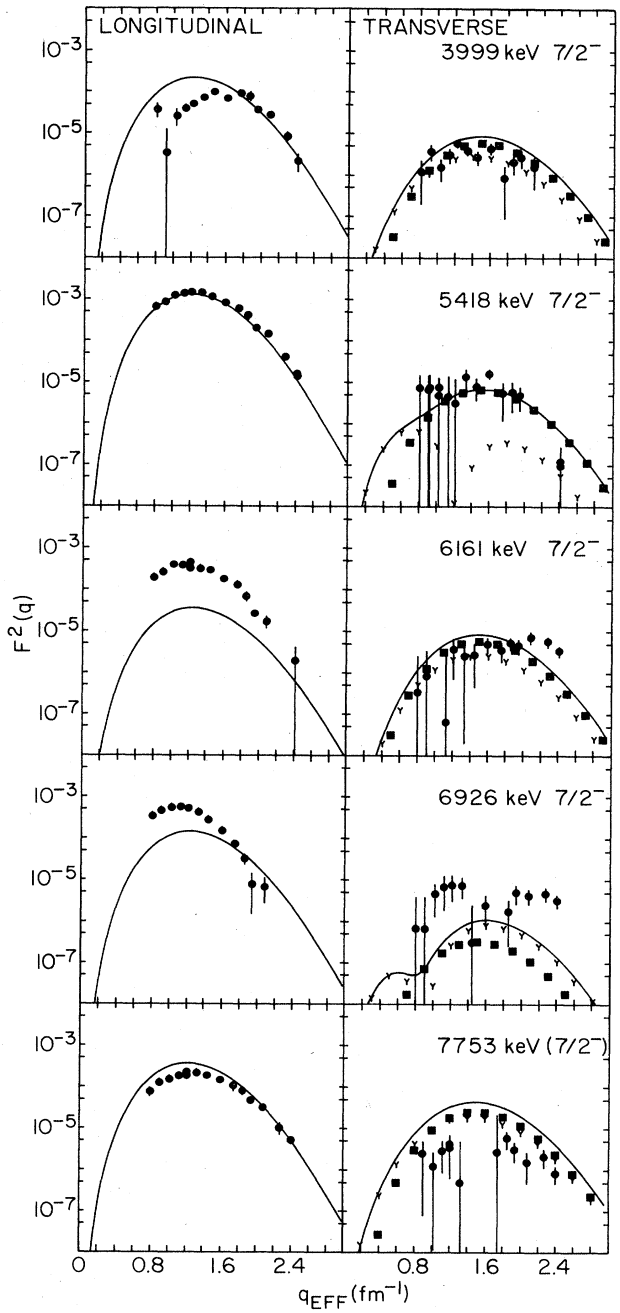

FIG. 14. Experimental and theoretical form factors for the $\frac{7}{2}^-$ levels observed in ^{19}F at 3.999, 5.418, 6.161, 6.926, and, perhaps, 7.753 MeV. Experimental values are indicated by the filled circles. The solid curves are the predictions for the first (3.999 MeV level), second (5.418 MeV level), third (6.161 MeV level), fourth (6.926 MeV level), and fifth (7.753 MeV level) PSD $\frac{7}{2}^-$ states of ^{19}F. The "Y" and "square" symbols in the transverse panels indicate, respectively, the separate $E3$ and $M4$ contributions to these form factors.

longitudinal component disagrees with theory at smaller values of momentum transfer. The second level, at 5.418 MeV, has a very large longitudinal component, in excellent agreement with the $E3$ predictions for the second PSD $\frac{7}{2}^-$. The corresponding transverse form factor is quite weak, again in agreement with the PSD prediction. The experimental longitudinal values for the third and fourth $\frac{7}{2}^-$ levels, while smaller than those of the second, are much larger than the predictions for the third and fourth PSD $\frac{7}{2}^-$ states. Also the shapes exhibit too much strength at lower q values. The longitudinal data for the 7.753 MeV level are consistent in magnitude and shape with the predictions for the fifth PSD $\frac{7}{2}^-$ state. In all of these cases, the experimental transverse form factor values

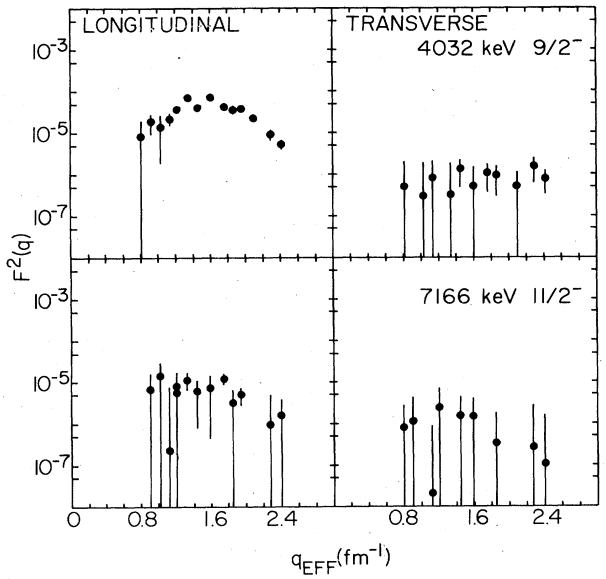

FIG. 15. Experimental form factors for the $\frac{9}{2}^-$ and $\frac{11}{2}^-$ levels observed in ^{19}F at, respectively, 4.032 and 7.166 MeV. Experimental values are indicated by the filled circles.

are so small as to be only marginally measurable. The PSD predictions are consistent with these small values.

A $\frac{9}{2}^-$ level is identified in ^{19}F at 4.032 MeV and an $\frac{11}{2}^-$ level at 7.166 MeV. The form factor data are shown in Fig. 15. Only the $\frac{9}{2}^-$ longitudinal component is appreciable. The only contribution to these transitions within the PSD space is the transverse ($M4$) component of the $\frac{9}{2}^-$. It is predicted to be much smaller than the small observed form factor.

VII. SUMMARY AND CONCLUSIONS

Many of the features of the scattering of intermediate energy electrons from ^{19}F which were observed in the present experiment have been found to be consistent overall with the predictions obtained from shell-model calculations for this nucleus. The observed phenomena which were analyzed consist of the distributions with respect to excitation energy and momentum transfer of the probabilities for longitudinal electric and transverse electric and magnetic excitation of multipolarities one through five. The theoretical wave functions with which the positive-parity levels are analyzed were obtained from an $(sd)^3$ space (SD model), while the wave functions used to analyze the negative-parity levels were generated in the space of four-particle (sd shell), one-hole (p shell) configurations. The shell-model predictions are obtained by combining the one-body densities obtained from the multiparticle configuration-mixing amplitudes with single-nucleon form factors and effective-charge renormalizations taken from analyses of heavier doubly-even sd-shell nuclei.

The spectrum of positive-parity longitudinal excitations is dominated at higher momentum transfer by the $\frac{1}{2}^+$, $\frac{5}{2}^+$, $\frac{3}{2}^+$, and $\frac{9}{2}^+$ members of the "ground-state rotational band." At lower momentum transfers the $\frac{9}{2}^+$ state is weaker and the $\frac{3}{2}^+$ and $\frac{5}{2}^+$ levels at 6.528 and 5.535 MeV are the next most prominent transitions. We note that the $\frac{9}{2}^+$ level is reached by $C4$ multipolarity, while the $\frac{5}{2}^+$ and $\frac{3}{2}^+$ levels are excited by $C2$. The lowest observed levels of each spin are obviously to be associated with the lowest calculated states of these spins, and the levels observed at 6.528 and 5.535 MeV clearly seem to correspond to the second $\frac{3}{2}^+$ and $\frac{5}{2}^+$ states in the SD model. The absolute magnitudes, the shapes (momentum transfer dependence), and the energy locations of these transitions are well accounted for by the SD model results.

The 6.528 and 5.535 MeV levels are the fifth $\frac{3}{2}^+$ and fourth $\frac{5}{2}^+$ levels actually observed in ^{19}F. The extra observed states are interpreted as excitations of many-hole, many-particle configurations across the ^{16}O shell closure. This interpretation is consistent with the results of shell-model calculations for this sort of effect. These states are relatively weakly excited in electron scattering, consistent with this interpretation, and tend to have shapes which are irregular and anomalous in terms of simple excitation models.

The combination of SD levels and those arising from shell-crossing configurations is not so easily dealt with in the case of $\frac{7}{2}^+$ levels. The lowest observed $\frac{7}{2}^+$ level, at 4.378 MeV, is very weakly excited and probably is best to be associated with the lowest SD model $\frac{7}{2}^+$ state at 4.871 MeV. However, the discrepancy in energies and the remaining ambiguities about the higher $\frac{7}{2}^+$ levels makes even this correspondence less than certain. There are three $\frac{7}{2}^+$ states in the $(sd)^n$ model below 8 MeV excitation energy, the third predicted to have very small form factors. There are at least five or six observed levels of this assignment in the same region. On the basis of the calculated and observed longitudinal form factors ($C4$ in this instance), and equally so when considering the transverse form factors, it is not possible unambiguously to associate any one of the next three observed levels with the second model state, even though all of the measured shapes have some congruence with the model prediction. It would seem that the SD form factor is spread among all three states, although there is not enough to go around in the present prediction.

In summary, theory agrees with experiment in the overall magnitude and location of $C2$ and $C4$ longitudinal strength from the ground state of ^{19}F. The $C2$ strength is found concentrated in the first 1.5 MeV of excitation energy, with a small secondary concentration in the 5.5—6.5 MeV region. The $C4$ strength is spread from 3 to 6 MeV, with the dominant contribution occurring in the lowest $\frac{9}{2}^+$ level. The observed momentum transfer dependence of these processes in the range studied is also well accounted for by the shell-model predictions.

The transverse form factors for the levels prominent in the longitudinal spectra of the positive-parity levels tend to confirm the assumed correspondences between experi-

mental and theoretical states and to exacerbate the ambiguities of the uncertain associations. The shapes and magnitudes of these form factors are also well reproduced by the theory, although not quite at the accuracy of the longitudinal results. The states strong in longitudinal scattering tend to be strong in transverse scattering as well. The transverse transitions proceed by mixtures of $M1$ and $E2$ ($\frac{3}{2}^+$), $E2$ and $M3$ ($\frac{5}{2}^+$), $M3$ and $E4$ ($\frac{7}{2}^+$), and $E4$ and $M5$ ($\frac{9}{2}^+$). The $\frac{11}{2}^+$ states can be reached only by $M5$ in the models we use here. The transverse scatterings were calculated with the free-nucleon values for the single-particle magnetic operators. The overall agreement in magnitudes between predictions and measurements indicates that the optimum effective values for these quantities are not very different from the free-nucleon values.

The transverse form factors are particularly important in understanding the higher-spin states. The ground state band $\frac{9}{2}^+$ and the $\frac{9}{2}^+$ level observed at 6.592 MeV excitation seem to be the only observed levels of this assignment below 8 MeV excitation. Their association with the two SD states calculated to occur at essentially the same energies is strengthened by the excellent agreement between the measured and calculated transverse form factors. Likewise, the large-q behavior in the transverse mode of the unresolved $\frac{3}{2}^+$, $\frac{11}{2}^+$ doublet observed at 6.50 MeV is a strong signature of the only $\frac{11}{2}^+$ state calculated below 8 MeV in the SD model.

The mixing of the various combinations of positive-parity electric and magnetic multipoles into the transverse transitions, and the frequent failures to obtain detailed agreement between predicted and measured shapes of individual form factors, makes it impossible to analyze in detail the accuracy of the predicted magnitudes and locations of the individual transverse multipole strengths. Overall, about the right amount of transverse strength is predicted for the lowest 8 MeV of excitation and the energy distribution is in reasonable accord with the experimental spectra.

The spectra of longitudinal excitations of negative-parity states in ^{19}F are dominated by the lowest $\frac{5}{2}^-$ state at 1.346 MeV excitation and $\frac{5}{2}^-$ and $\frac{7}{2}^-$ states at approximately 5.5 MeV. The shell-model calculations of the $E3$ strengths of the first and third $\frac{5}{2}^-$ states and the second $\frac{7}{2}^-$ state in the PSD spectrum give a good accounting of this strength in terms of the correct magnitudes and momentum-transfer dependence. The higher PSD $\frac{7}{2}^-$ states have, in the aggregate, less $E3$ strength than the appreciable amount observed for the experimental $\frac{7}{2}^-$ levels between 6 and 8 MeV. The other known and possible $\frac{5}{2}^-$ levels have very little strength, in agreement with the PSD predictions.

The observed transverse form factors for these $\frac{5}{2}^-$ and $\frac{7}{2}^-$ levels are smaller relative to their longitudinal values than is the case for the positive-parity levels. This is particularly true for the 5.5 MeV transitions, in which the strong longitudinal components are matched with almost vanishing transverse components. The PSD predictions correctly predict this effect, putting more transverse strength into the lowest $\frac{5}{2}^-$ and $\frac{7}{2}^-$ states than into the higher states and, overall, correctly predicting the magnitudes and shapes for all of these states.

In the transverse mode, the lowest $\frac{1}{2}^-$ level of ^{19}F is also prominent in the experimental spectrum. The PSD $E1$ prediction for the first $\frac{1}{2}^-$ state matches these data in magnitude and shape. The next most significant transverse $E1$ transition is observed for the $\frac{3}{2}^-$ level at 6.787 MeV, in agreement with the prediction for the fourth PSD $\frac{3}{2}^-$ state.

None of the $\frac{1}{2}^-$ and $\frac{3}{2}^-$ states is predicted to have a large longitudinal form factor. This is in rough agreement with observation. The predicted form factors do not reproduce the trends of the form factors at low momentum transfers, where the experimental strengths are considerably larger than the model shapes predicts. These disagreements at low q, for transitions of at least modest strength to well identified and isolated levels, seem to constitute the most systematic and significant failures of the shell-model calculations to account for the present measurements.

In dealing with the significant excess of $\frac{1}{2}^+$, $\frac{3}{2}^+$, $\frac{5}{2}^+$, and $\frac{7}{2}^+$ levels observed in ^{19}F over the SD model predictions, the following conclusions emerge: For the $\frac{3}{2}^+$ and $\frac{5}{2}^+$ cases, an approximate distinction between the SD and intruder states can be established, with the intruder levels having weak and partially anomalous form factors and the SD levels being relatively stronger and well accounted for in the SD theory. The $\frac{7}{2}^+$ levels appear to be seriously intermixed, however, and cannot be understood quantitatively with the current calculations. The $\frac{1}{2}^+$ levels cannot be treated definitively and the $\frac{9}{2}^+$ and $\frac{11}{2}^+$ levels are uncomplicated and in good agreement with the SD predictions.

We conclude that the detailed distributions of multipole strength with respect to excitation energy obtained from the shell model calculations for ^{19}F studied here are confirmed by the present measurements. Also, the observed magnitudes of these strengths are in agreement with predictions which incorporate the standard effective charge and moment renormalizations for the various electromagnetic operators. The detailed form factor shapes observed for the stronger transitions are typically well matched by the theoretical predictions.

The PSD calculations give an excellent accounting for the distribution and shapes of longitudinal $E3$ strength in $\frac{5}{2}^-$ and $\frac{7}{2}^-$ levels and for the relative proportions of longitudinal and transverse strength from state to state. They cannot account for the observed longitudinal behavior of the $\frac{1}{2}^-$ and $\frac{3}{2}^-$ levels at smaller q values, although they do account reasonably well for the transverse features of these states.

The present theoretical solutions for ^{19}F seem to account for the features observed in this experiment at least as well as could have been expected in the light of their disjoint origins. The next level of analysis needs to be based on positive parity wave functions in which multiparticle, multihole components are coexistent with the SD configurations and negative-parity wave functions which incorporate both multiparticle, multihole components and fp-shell excitations in addition to the PSD

configurations. The success of the present hybrid approach suggests that a successful integration of these structural features should give an excellent accounting of the present experimental phenomena, with the $C1$ longitudinal features constituting probably the biggest challenge.

ACKNOWLEDGMENTS

The Michigan State University group was supported in part by NSF Grant PHY-83-12245. The Catholic University group was supported in part by NSF Grants PHY-79-23968 and PHY-82-107076. The MIT group was supported in part by DOE Contract EY-76-C-02-3069.

APPENDIX A: THE TRANSVERSE MAGNETIC SINGLE-PARTICLE MATRIX ELEMENTS

After some manipulation of the vector algebra the transverse magnetic (TM) single-particle matrix elements can be written in the form[24,26]

$$w(MLc,q,j,j',t_z)=2i\{1/[L(L+1)]^{1/2}\}\int\langle j,t_z||\{[L/(2L+1)]^{1/2}\mathbf{M}(L,L-1,q,\mathbf{r}) +[(L+1)/(2L+1)]^{1/2}\mathbf{M}(L,L+1,q,\mathbf{r})\}\cdot\mathbf{l}(\mathbf{r},t_z)||j',t_z\rangle d^3r \tag{A1}$$

and

$$w(MLm,q,j,j',t_z)=(iq/2)\int\langle j,t_z||\{[(L+1)/(2L+1)]^{1/2}\mathbf{M}(L,L-1,q,\mathbf{r}) -[L/(2L+1)]^{1/2}\mathbf{M}(L,L+1,q,\mathbf{r})\}\cdot\boldsymbol{\sigma}(\mathbf{r},t_z)||j',t_z\rangle d^3r\ , \tag{A2}$$

where $\mathbf{l}$ and $\boldsymbol{\sigma}$ are the orbital and spin operators

$$\mathbf{l}(\mathbf{r},t_z)=\sum_k P_k(t_z)g_l(t_z)u_N(-i/2)\{\mathbf{r}\times[\nabla_k\delta(r-r_k)+\delta(r-r_k)\nabla_k]\}\ , \tag{A3}$$

$$\boldsymbol{\sigma}(\mathbf{r},t_z)=\sum_k P_k(t_z)g_s(t_z)u_N(\sigma_k/2)\delta(r-r_k)\ . \tag{A4}$$

These matrix elements have been reduced to a concise form by Arita[31] who obtains

$$w(MLc,q,j,j',t_z)=iqg_l(t_z)u_N\left[\int h(MLc^+,r,j,j',t_z)j_{L+1}(qr)r^2dr+\int h(MLc^-,r,j,j',t_z)j_{L-1}(qr)r^2dr\right] \tag{A5}$$

and

$$w(MLm,q,j,j',t_z)=iqg_s(t_z)u_N\left[\int h(MLm^+,r,j,j',t_z)j_{L+1}(qr)r^2dr+\int h(MLm^-,r,j,j',t_z)j_{L-1}(qr)r^2dr\right]\ , \tag{A6}$$

where

$$h(MLc^+,r,j,j',t_z)=h(MLc^-,r,j,j',t_z) =\{[L(L+1)]^{1/2}/(2L+1)\}C(ML,j,j')[1+B(j,j')/L][1-B(j,j')/(L+1)]D(r,j,j',t_z)\ , \tag{A7}$$

$$h(MLm^+,r,j,j',t_z)=\{-(\tfrac{1}{2})[L(L+1)]^{1/2}/(2L+1)\}C(ML,j,j')[1-B(j,j')/(L+1)]D(r,j,j',t_z) \tag{A8}$$

and

$$h(MLm^-,r,j,j',t_z)=\{-(\tfrac{1}{2})[L(L+1)]^{1/2}/(2L+1)\}C(ML,j,j')[1+B(j,j')/L]D(r,j,j',t_z) \tag{A9}$$

and where B and C are given by Eqs. (25) and (26), respectively. By integrating Eqs. (A5) and (A6) by parts and using the properties of the spherical Bessel functions, we obtain the results in the form of Eqs. (16) and (17) where

$$h(MLc,r,j,j',t_z)=dh(MLc^+,r,j,j',t_z)/dr+(L+2)(1/r)h(MLc^+,r,j,j',t_z) -dh(MLc^-,r,j,j',t_z)/dr+(L-1)(1/r)h(MLc^-,r,j,j',t_z)\ , \tag{A10}$$

$$h(MLm,r,j,j',t_z)=dh(MLm^+,r,j,j',t_z)/dr+(L+2)(1/r)h(MLm^+,r,j,j',t_z) -dh(MLm^-,r,j,j',t_z)/dr+(L-1)(1/r)h(MLm^-,r,j,j',t_z)\ . \tag{A11}$$

Substituting Eqs. (A7)—(A9) one obtains the results given in Eqs. (16) and (17).

APPENDIX B: RELATIONSHIP WITH THE NOTATION OF DONNELLY AND HAXTON

From the expressions for the transition densities derived in this work, the coefficients given in tabular form by Donnelly and Haxton[32] can be reduced to simple expressions involving only a three-j symbol. The new results arise mainly from the new expressions given for the transverse magnetic form factor. However, for completeness we give below the

complete mapping between our coefficients $C[(E/M)L,j,j']$ [Eq. (26)] and $B(j,j')$ [Eq. (25)] and the coefficients A_L, B_L, C_L, D_L, and E_L of Donnelly and Haxton:

$$A_L(j,j')=(4\pi)^{1/2}C(EL,j,j') ,$$

$$B_L(j,j')=-(4\pi)^{1/2}(\tfrac{1}{2})[L(L+1)(2L+1)]^{1/2}C(EL,j,j')[1+B(j,j')/L][1-B(j,j')/(L+1)] ,$$

$$C_L(j,j')=(4\pi)^{1/2}(\tfrac{1}{2})[L(L+1)]^{-1/2}C(EL,j,j') ,$$

$$D_L(j,j')=(4\pi)^{1/2}[L(L+1)]^{-1/2}C(EL,j,j')[j(j+1)-j'(j'+1)-l(l+1)+l'(l'+1) ,$$

$$D_L^+(j,j')=(4\pi)^{1/2}[(L+1)^{1/2}/(2L+1)]C(ML,j,j')[1-B(j,j')/(L+1)] ,$$

$$D_L^-(j,j')=-(4\pi)^{1/2}[(L)^{1/2}/(2L+1)]C(ML,j,j')[1+B(j,j')/L] ,$$

$$E_L(j,j')=-(4\pi)^{1/2}C(ML,j,j') .$$

From these relations it is easy to verify Eqs. (6) of Ref. 32.

APPENDIX C: CONVERSION BETWEEN THE MULTIPARTICLE TRANSITION AMPLITUDES IN ISOSPIN AND PROTON-NEUTRON FORMALISM

With wave functions which have good isospin, it is often convenient to calculate the multiparticle transition amplitudes in isospin formalism

$$A^{\Delta T}(L,j,j',f,i)=[(2L+1)(2\Delta T+1)]^{-1/2}\langle f|||[a^\dagger(j)\otimes\tilde{a}(j')]^{(L,\Delta T)}|||i\rangle . \tag{C1}$$

It is straightforward to use these to obtain the multiparticle transition amplitudes in proton-neutron formalism [Eq. (37)] for a given value of T_Z

$$A[L,j,j',f,i,T_Z,t_z=(\pm)\tfrac{1}{2}]=(-1)^{T_f-T_Z}\left[(2)^{1/2}\begin{pmatrix} T_f & 0 & T_i \\ -T_Z & 0 & T_Z \end{pmatrix}A^{\Delta T=0}(L,j,j',f,i)/2 \pm(6)^{1/2}\begin{pmatrix} T_f & 1 & T_i \\ -T_Z & 0 & T_Z \end{pmatrix}A^{\Delta T=1}(L,j,j',f,i)/2\right] . \tag{C2}$$

---

*Present address: Department of Physics, Drexel University, Philadelphia, PA 19104.

†Present address: Fermilab, Batavia, IL 60510.

[1]P. L. Hallowell, W. Bertozzi, J. Heisenberg, S. Kowalski, X. Maruyama, C. P. Sargent, W. Tuchinetz, C. F. Williamson, S. P. Fivozinsky, J. W. Lightbody, and S. Penner, Phys. Rev. C **7**, 1396 (1973).

[2]M. Oyamoda, T. Terasawa, K. Nakahara, Y. Endo, H. Saito, and E. Tanaka, Phys. Rev. C **11**, 1578 (1975).

[3]W. Bertozzi, M. V. Hynes, C. P. Sargent, C. Creswell, P. C. Dunn, A. Hirsch, M. Leitch, B. Norum, F. N. Rad, and T. Sasanuma, Nucl. Instrum. Methods **141**, 457 (1977).

[4]W. Bertozzi, M. V. Hynes, C. P. Sargent, W. Turchinetz, and C. F. Williamson, Nucl. Instrum. Methods **162**, 211 (1979).

[5]J. P. Elliott and B. H. Flowers, Proc. R. Soc. London **A229**, 536 (1955).

[6]M. G. Redlich, Phys. Rev. **99**, 1427 (1955).

[7]T. Walcher and P. Strehl, Z. Phys. **232**, 342 (1970).

[8]C. F. Williamson, F. N. Rad, S. Kowalski, J. Heisenberg, H. Crannell, J. T. O'Brien, and H. C. Lee, Phys. Rev. Lett. **40**, 1702 (1978).

[9]P. H. Stelson and F. K. McGowen, Nucl. Phys. **16**, 92 (1960).

[10]A. E. Litherland, M. A. Clark, and C. Broude, Phys. Lett. **3**, 204 (1963).

[11]J. A. Becker, J. W. Olness, and D. H. Wilkinson, Phys. Rev. **155**, 1089 (1967).

[12]T. K. Alexander, O. Hausser, K. W. Allen, and A. E. Litherland, Can. J. Phys. **47**, 2335 (1969).

[13]A. R. Poletti, J. A. Becker, and R. E. McDonald, Phys. Rev. **182**, 1054 (1969).

[14]W. Bertozzi, J. Haimson, C. P. Sargent, and W. Turchinetz, IEEE Trans. Nucl. Sci. **NS-14**, 191 (1967).

[15]Teflon is a trade mark of E. I. duPont de Nemours and Co.

[16]P. C. Dunn, S. B. Kowalski, F. N. Rad, C. P. Sargent, W. E. Turchnetz, R. Goloski, and D. P. Saylor, Phys. Rev. C **27**, 71 (1983); P. C. Dunn, Ph.D. thesis, Harvard University, 1980.

[17]F. Ajzenberg-Selove, Nucl. Phys. **A392**, 1 (1983).

[18]J. C. Bergstrom, MIT 1967 Summer Study, Medium Energy Nuclear Physics with Electron Accelerators, 1967, p. 251.

[19]J. C. Bergstrom, private communication

[20]L. W. Mo and Y. S. Tsai, Rev. Mod. Phys. **41**, 205 (1965).

[21]L. Maximon and D. B. Isabelle, Phys. Rev. **136**, B674 (1964).

[22]H. Uberall, *Electron Scattering from Complex Nuclei* (Academic, New York, 1971).

[23]J. L. Friar and J. W. Negele, Adv. Nucl. Phys. **8**, 219 (1975).

[24]R. S. Willey, Nucl. Phys. **40**, 529 (1963).

[25]T. De Forest and J. D. Walecka, Adv. Phys. **15**, 1 (1966).

[26]T. W. Donnelly and J. D. Wakecka, Nucl. Phys. **A201**, 81 (1973); Annu. Rev. Nucl. Sci. 25, 329 (1975).

[27]A. R. Edmonds, *Angular Momentum in Quantum Mechanics* (Princeton University Press, Princeton, 1960).

[28]A. de-Shalit and I. Talmi, *Nuclear Shell Theory* (Academic,

New York, 1963).
[29]M. Abromowitz and I. A. Stegun, *Handbook of Mathematical Functions* (Dover, New York, 1965).
[30]T. W. Donnelly and W. C. Haxton, At. Data Nucl. Data Tables **23**, 103 (1979).
[31]K. Arita, Genshikaku Kenkyu **22**, 119 (1977).
[32]T. W. Donnelly and W. C. Haxton, At. Data Nucl. Data Tables **25**, 1 (1980).
[33]P. J. Brussaard and P. W. M. Glaudemans, *Shell-Model Applications in Nuclear Spectroscopy* (North-Holland, Amsterdam, 1977).
[34]A. J. F. Siegert, Phys. Rev. **52**, 787 (1937).
[35]D. Cha, Phys. Rev. C **21**, 1672 (1980).
[36]J. D. Jackson, *Classical Electrodynamics* (Wiley, New York, 1962), p. 556.
[37]J. L. Friar and S. Fallieros, Phys. Lett. **114B**, 403 (1982).
[38]L. J. Tassie and F. C. Barker, Phys. Rev. **111**, 940 (1958).
[39]H. Chandra and G. Sauer, Phys. Rev. C **13**, 245 (1976).
[40]B. A. Brown, W. Chung, and B. H. Wildenthal, Phys. Rev. C **22**, 774 (1980).
[41]B. H. Wildenthal, in Proceedings of the International School of Nuclear Physics, 7th course, Mesons, Isobars, Quarks and Nuclear Excitations, Erice-Trapani-Sicily, 1983; *Progress in Particle and Nuclear Physics*, edited by D. H. Wilkinson (Pergamon, London, 1984), Vol. 11, p. 5.
[42]D. J. Millener and D. Kurath, Nucl. Phys. **A255**, 315 (1975).
[43]B. M. Preedom and B. H. Wildenthal, Phys. Rev. C **6**, 1633 (1972).
[44]S. Cohen and D. Kurath, Nucl. Phys. **73**, 1 (1965).
[45]D. H. Gloeckner and R. D. Lawson, Phys. Lett. **53B**, 313 (1974).
[46]B. S. Reehal and B. H. Wildenthal, Part. Nucl. **6**, 137 (1973).
[47]A. P. Zuker, B. Buck, and J. B. McGrory, Phys. Rev. Lett. **21**, 39 (1968).
[48]A. P. Zuker, Phys. Rev. Lett. **23**, 893 (1969).
[49]M. V. Hynes, private communication.
[50]L. A. Schaller, T. Dubler, K. Kaesser, G. A. Rinker, B. Robert-Tissot, L. Schellengberg, and H. Schneuwly, Nucl. Phys. **A300**, 225 (1978).
[51]B. A. Brown, R. Radhi, and B. H. Wildenthal, Phys. Rep. **101**, 314 (1983).
[52]H. Sagawa and B. A. Brown, Nucl. Phys. **A430**, 84 (1984); Phys. Lett. **150B**, 247 (1985).
[53]L. J. Tassie, Aust. J. Phys. **9**, 407 (1956).
[54]B. A. Brown, R. Radhi, and B. H. Wildenthal, Phys. Lett. **B133**, 5 (1983).